FORCE MODELING IN DRILLING WITH APPLICATION TO BURR MINIMIZATION

A Thesis
Presented to
The Academic Faculty

by

Jennifer Rose Flachs

In Partial Fulfillment
of the Requirements for the Degree
Master of Science in the
George W. Woodruff School of Mechanical Engineering

Georgia Institute of Technology
December 2011

FORCE MODELING IN DRILLING WITH APPLICATION TO BURR MINIMIZATION

Approved by:

Professor Shreyes Melkote, Advisor
George W. Woodruff School of Mechanical Engineering
Georgia Institute of Technology

Professor Steven Danyluk
George W. Woodruff School of Mechanical Engineering
Georgia Institute of Technology

Professor Steven Liang
George W. Woodruff School of Mechanical Engineering
Georgia Institute of Technology

Date Approved: 10 November 2011

To my family and friends,

Without your love and support this never would have been possible.

ACKNOWLEDGMENTS

I owe a great deal to the following, whose assistance during my time at Georgia Tech was invaluable.

- Dr. Shreyes Melkote, my advisor, who helped me to always make progress
- John Morehouse, our research engineer
- Lockheed Martin Corp. for their sponsorship of this research
- Dr. Steven Danyluk and Dr. Steven Liang, my committee members
- Steven Sheffield, for dropping what he was doing to help me out on numerous occasions
- All the students of the FMPR, especially Mukund, George and Craig
- Jordan and Elise
- All my salseros and bachateros
- My parents and my sisters

Without you, I would still be working on this.

TABLE OF CONTENTS

LIST OF TABLES

LIST OF FIGURES

SUMMARY

In the aerospace industry, burr removal is a very important part of the manufacturing process. Stacks of material on sections of an aircraft are assembled and drilled by hand. Due to extensive burr formation the sheets must be destacked so that burrs can be removed and then the stacks are reassembled and fastened together. If burrs are minimized in the drilling process, this would reduce the necessity for the sheets to be destacked and deburred.

One approach to minimizing burrs is to lower the thrust force in drilling through suitable modification of the drill geometry such as the use of a step drill. Although prior researchers have analyzed different drill geometries such as step drills and their effect on hole exit burr formation in the drilling process through experimentation, no work has been reported on modeling and analysis of step drilling forces and their relationship to burr formation as a function of the step drill geometry parameters. Consequently, this thesis focuses on the modeling of the thrust force and torque for step drills and analyzes their relationship with burr size as a function of the step drill geometry parameters. In the first step, a mechanistic model for thrust and torque in drilling is implemented for a standard twist drill. This mechanistic model is then adapted to predict the thrust and torque for a step drill. Subsequently, experiments are performed to validate the mechanistic model and to evaluate burr formation with standard and step drills. The influence of thrust and torque on hole exit burr formation is analyzed for different step drill geometries and experimental feeds and speeds. The results show that the predicted thrust and torque values for both drill geometries are in good agreement with measured values, although the torque model consistently underpredicts. For standard drill geometry in the calibration tests, the

average error in the thrust prediction is 7.09% and the average error in the torque prediction is -18.05%. In validation tests, the average error for predicted thrust is 2.29% and the average error for predicted torque is -18.46%. For the step drill model the average error in thrust is 0.72% while the average error in torque is -8.72%. In addition, a reduction in the predicted thrust force for a step drill relative to the standard twist drill is found to correlate well with a reduction in the measured burr size. However, further reduction in the thrust force by varying the step angle and diameter ratio do not correlate well with the measured burr size. Likely reasons for these results are presented in this thesis.

CHAPTER I

INTRODUCTION

1.1 Background and Motivation

In the aerospace industry, drilling is performed on many sections of large aircraft, resulting in millions of through-holes. When drilling through ductile materials burrs are formed at the entry and exit of a hole as a result of plastic deformation. These burrs have sharp, uneven edges and are usually undesirable. Depending on the part specifications, the burrs may need to be removed, but the removal process is very expensive and time consuming. If the burrs are not removed they could cause potential problems including misalignment of parts or become a source of crack propagation and fatigue failure in parts subjected to cyclic loading. In prior works, researchers have proposed that a reduction in thrust force in drilling will reduce exit burr height. If the thrust and the torque for the drilling process is accurately modeled, then the effect of drill geometry and process parameters on thrust and torque can be studied. In using this model, the relationship between thrust and torque and burr height can also be investigated.

1.2 Objective

The primary objective of this thesis is to develop, calibrate and validate a mechanistic force model for drilling that is then adapted to predict the thrust and torque produced when drilling with a step drill. Another goal is to use the developed mechanistic model to investigate the effect of varying step drill geometry and drilling speed and feed on thrust and torque. The final objective of this work is to use the developed mechanistic model with experiments to investigate the relationship between burr height and thrust

and torque.

1.3 Thesis Outline

Chapter two contains an overview of standard and step drill geometries followed by descriptions of drill geometries used by other researchers when analyzing the effect of different geometries on burr formation and a discussion of drill materials. Next, different approaches to modeling thrust and torque when drilling are described. This chapter is concluded with a discussion of the types of burrs and a review of currently used models of burr formation in drilling.

In the third chapter the drilling force model is developed. Different cutting mechanisms occurring on the cutting lips and chisel edge are presented, followed by the modification of the model to predict the thrust and torque produced when drilling with a step drill. Chapter four discusses the calibration procedure for the model of the standard twist drill as well as validation for the standard and step drill models.

Chapter five focuses on the measurement and analysis of the burrs produced in drilling. The measurement procedure is introduced, followed by studies on the impact of different step drill geometry characteristics and experimental parameters on burr height. The thesis is concluded with a chapter containing the conclusions and recommendations based on the results of the work contained herein.

CHAPTER II

LITERATURE REVIEW

This chapter contains an overview of drilling geometry noting the characteristics of a standard drill and the modifications that are done to a standard drill in order to form a step drill. Prior work focused on modeling the forces in drilling is then described as well as investigations of burr formation.

2.1 Overview of Drill Geometry

The most common type of drill used is the jobber drill. Jobber drills are shaped such that the length of the flutes is four of five times the diameter of the drill and the shank of the drill is the same diameter of the body as shown in Figure 1. The point of a drill contains the cutting edges while the body of the drill contains the flutes which allow for chip evacuation.

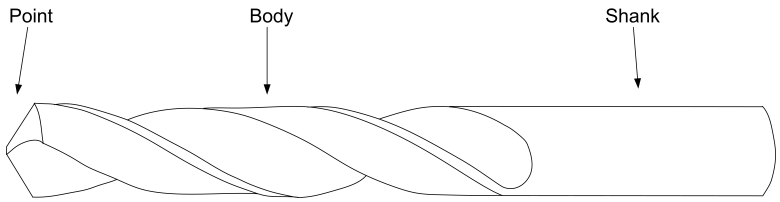

Figure 1: Jobber Drill

The geometry of the point and body of a standard twist drill are defined by the quantities in Figure 2. The cutting areas on the point of the drill are the cutting lips and chisel edge. The flutes are cut away from the body of the drill and meet the clearance face to form the cutting lips. The helix angle (α_{hxo}) of a drill is specified at the diameter of a drill and is measured in reference to the drill axis. The helix angle is determined so that the flutes meet the clearance face in such a way that the

cutting lips are straight. The diameter of the drill (D) is measured across the widest part of the drill, at the margins. The radius of the drill (R) is specified as one half of the drill diameter.

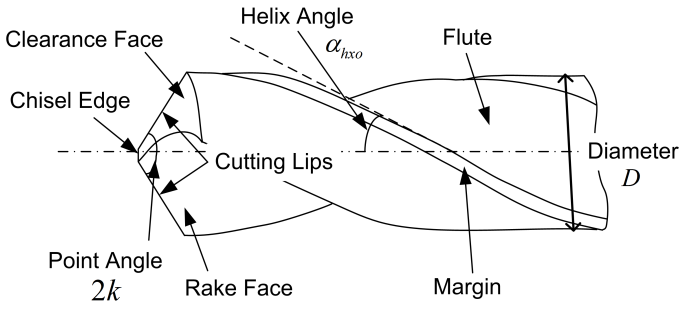

Figure 2: Jobber Drill Point and Body

2.1.0.1 Drill Point

The point of the drill contains the cutting edges and the rake and clearance faces. There are two different cutting edges on the drill, the cutting lips and chisel edge. The cutting lips are located off-center, parallel to one another and are connected by the chisel edge. The angle between the cutting lips is the point angle of the drill ($2k$). The normal distance between the cutting lips is specified as the web thickness ($2w$) as shown in Figure 3. The chisel edge angle (ψ) is the angle between one of the cutting lips and the chisel edge, measured in a plane normal to the drill axis.

The web is thinnest at the end of the drill and is larger within the body of the drill. If a drill is reground multiple times the web thickness will increase, but the chisel edge angle will remain unchanged.

The cutting lips do not intersect the axis of the drill, so the instantaneous radius (r) is identified in relation to the inclination angle ($i(r)$) as defined in Equation 1.

$$i(r) = \sin^{-1}\left(\frac{w}{r\ \sin(k)}\right) \tag{1}$$

The helix angle (α_{hxo}) is specified at the diameter of a drill, but its value changes along a drill's radius. The instantaneous helix angle ($\alpha_{hx}(r)$) can be determined as

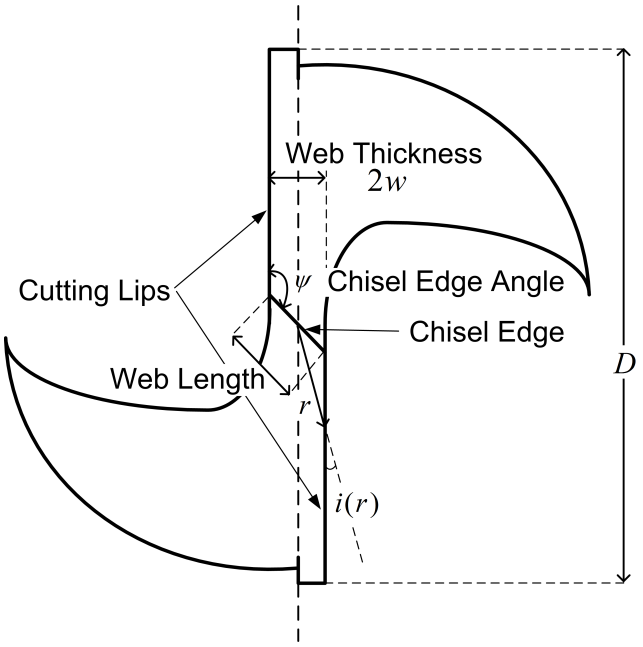

Figure 3: Drill Point

shown in Equation 2.

$$\alpha_{hx}(r) = \tan^{-1}\left(\frac{2r\ \tan\ \alpha_{hxo}}{D}\right) \tag{2}$$

The inclination angle and helix angle are used to determine the normal rake angle ($\alpha_n(r)$) along the cutting lips as shown in Equation 3 [2]. The normal rake angle is the angle between the workpiece and the cutting face of the drill measured in a plane perpendicular to the cutting edge; it is dependent on the instantaneous radius.

$$\alpha_n(r) = \tan^{-1}\left(\tan\ \alpha_{hx}(r)\ \cos\ i(r)\right) \tag{3}$$

2.1.1 Step Drill Geometry

Step drills are very similar to standard jobber drills with two main differences. Instead of the cutting lips of a drill extending from the chisel edge to the drill radius, they are separated into two sections. The innermost section, designated the primary point angle (or simply 'point angle') extends from the chisel edge to a radial value less than the drill radius (R) as shown in Figure 4. This region is known as the inner diameter (iD). At the conclusion of the primary point angle, the diameter of the drill remains

constant at the value of the inner diameter for a length along the axis of the drill defined as the step length (L). After the step length, the secondary point extends from the inner diameter (iD) to the drill diameter (D) at an angle known as the step angle or secondary point angle ($2sk$). It is customary to add an undercut where the step angle meets the inner diameter to prevent the radius at this transition from cutting.

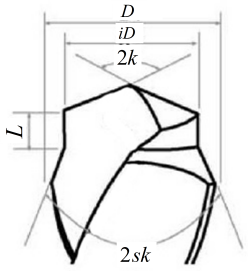

Figure 4: Step Drill Geometry

2.1.2 Other Drill Geometries

This thesis focuses on standard and step drill geometries, however other geometries are described here to aid in comparison of the results in this study with those of other researchers using these geometries. Some of the more common types include the split point, chamfer, round, carbide and double point-angle drills. Figure 5 displays drill geometries investigated by Ko et al. [14].

High speed steel and carbide drills are standard and widely available. Chamfer drills have a chamfer at the corner edge, designated by the chamfer length and the chamfer angle while round drills have a radius at the outer edge of the cutting lips. In the investigation by Ko et al. the step drills used contain a split point which is the result of cutting away a portion of the rake face on the chisel edge. The double point angle drill was investigated by López de Lacalle et al. [4] and is shown in Figure 6.

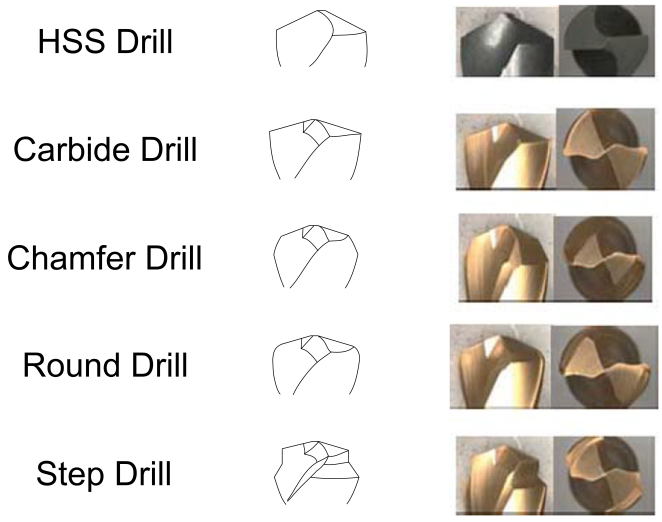

Figure 5: Drill Geometries Investigated by Ko et al. {adapted from [14]}

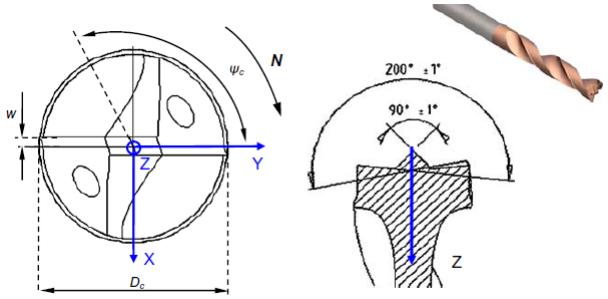

Figure 6: Double Point Angle Drill Investigated by López de Lacalle et al. [4]

2.2 Drill Materials

Typical drill materials include low carbon steel, high carbon steel, high speed steel and cobalt steel alloys. Other less common materials include carbides (such as tungsten carbide) and polycrystalline diamond. The drill material is chosen based on the workpiece material. Low carbon steel is only used to drill wood while cobalt steel alloys are used to drill hard materials such as stainless steel. High speed steel drills can be used on a variety of workpiece materials including hardwood, metals and other materials. Some drills are coated to improve tool life. In this thesis the drills used

are high speed steel with a black oxide coating. In the following section, the focus is shifted from the drills themselves to an analysis of the drilling process.

2.3 Thrust and Torque Modeling

Past research has approached modeling the forces produced in drilling by empirical, mechanistic and finite element methods. Empirical models were first implemented to investigate the relationship between thrust, torque and different parameters. This approach was followed by a mechanistic approach which requires more knowledge of the kinematics of a process. The finite element approach is the most recent method, requiring more mathematical models but fewer experiments. The purposes for modeling are varied and depend on the researcher's goals. Armarego [1] formed a "generic mechanics" approach to cutting for the purposes of optimizing economic performance. By decreasing the thrust and torque when drilling he aimed to reduce the required power and improve the tool-life. Reducing power, improving tool-life and reducing deflection are also the foci of many other works [4] [22] [25] [26].

2.3.1 Empirical Approach

In empirical modeling, experiments are designed with input parameters determined using statistical tools, such as a Box-Behnken design or Taguchi array, so that the effect of the inputs on the thrust and torque can be determined. This type of experimental approach can be very time consuming and expensive [1]. Typical inputs investigated are point angle, feed and speed and they are usually tested at a few values. Because the relationship between the inputs and the thrust and torque is unknown, it is usually approximated by a low order polynomial. This approximation puts a limitation on the predictive application of the empirical model. As the true relationship between the inputs and outputs may not be a polynomial, the errors in modeling may increase outside of the tested region.

Xia and Mahdavian [27] created empirical models for step drills using a power

law relationship between inputs (speed, feed and diameter) and outputs (thrust and torque) and separated the inner and outer diameter into two separate models. In their work the thrust produced by the step drills was greater than that produced by the standard twist drills, potentially due to an increase in web thickness resulting from the procedure used to grind the step. They also came to the conclusion that the inner diameter should not be less than 60% of the outer diameter of the drill so cutting speeds of the inner portion of the drill would be within the range of recommended speeds for drill performance.

2.3.2 Mechanistic Approach

The mechanistic modeling approach can be considered an improvement over the empirical approach because it involves more knowledge of the process instead of fitting equations by a multivariable regression analysis. An understanding of the kinematics of a process is required as well as the basic assumption that the cutting forces are proportional to the uncut chip area or chip load [10]. The material characteristics are included within calibration constants obtained experimentally, while the kinematics are explicitly modeled. Because of the improved understanding of the physics of the process, fewer calibration experiments are required than for the empirical approach and it is more likely that the model will be valid outside of the tested range with reasonable errors. When forming a mechanistic model for drilling, the cutting lips are separated from the chisel edge because of the different cutting methods in each region. Research performed by Oxford Jr. established that there are two regions on the chisel edge of the drill, an indentation zone at the center and a secondary cutting zone outside of the indentation zone [20]. The cutting lips remove material by oblique cutting while the secondary cutting zone on the chisel edge performs orthogonal cutting.

A mechanistic model for predicting thrust and torque was developed by Chandrasekharan [2] that was accurate within 15% for most experimental inputs. This

model is the basis for the force model developed and improved upon in this thesis.

Gong et al. [6] performed a study focusing directly on the point when the drill contacts the workpiece. Drill skidding and wandering is investigated using this model that includes a dynamic chip thickness, which is calculated as a result of tool deflections and drill grinding errors. The dynamic chip thickness is not implemented into the mechanistic model described in this study in order to reduce calculation time and because the simplified static chip thickness gives sufficient accuracy in modeling.

2.3.3 Finite Element Approach

The finite element method (FEM) has been used since the 1960's, making it the most recent of the three approaches discussed here [3]. With this approach, the researcher uses mathematical models to define the flow stress, failure criteria, and contact relationships between the workpiece and cutting tool and very powerful software to simulate the process. Three software programs commonly used to perform finite element analysis are Abaqus, AdvantEdge and Deform.

When using these software, the tool and workpiece are chosen from a library within the software, designed within the software, or built using an outside CAD package and imported into the software. Material properties are then assigned to both the workpiece and cutting tool. Process conditions must then be determined, including environmental temperature, friction factors and heat transfer coefficients.

Two different meshing criteria are typically used for FEM analysis. The Lagrangian technique tracks discrete material points and the Eulerian style tracks volumes [17]. Lagrangian is more commonly used for finite element models in metal cutting. Once all of the parameters and relationships are determined the simulation is processed, which can be very time consuming. One of the benefits of FEM is that experiments are typically only necessary for validation purposes, as done by Isbilir and Ghassemieh [8].

2.4 Burr Formation

Most studies on burr formation focus explicitly on the burrs formed as the drill exits the workpiece as these are larger than the entrance burrs. Hence, throughout this thesis 'burrs' are assumed to be exit burrs unless specified as entrance burrs.

Experimental and finite element studies have been undertaken by many researchers to analyze the formation of exit burrs in drilling. Ko and Lee analyzed the burr formation produced by a new-concept drill developed by Hosoi in 1977 focusing on optimizing the geometry to reduce burr height [16]. In a later article burr formation was studied for step drills, carbide drills, round drills, chamfer drills and high speed steel (HSS) drills in four different workpiece materials; it was determined in this work that the step drill produced the smallest burrs [14]. In the work done by Kim and Dornfeld, burr thickness and height are modeled based on Merchant's shear plane model which does not account for cutting speed, but displayed reasonable agreement in the relationship between burr height and thickness and drill feed, point angle, and helix angle [13].

2.4.1 Types of Burrs

In earlier works studying the influence of input parameters on burr formation, the resulting burrs are classified into three types based on the initiation of the crack [15]. Type A burrs are very small and are formed on very brittle materials. The crack is initiated at the drill point and outer edge. Type B burrs can be formed with or without a cap and occur when the workpiece undergoes some plastic deformation. For type B burrs the crack initiates at the outer edge of the drill. Type C burrs occur when the crack begins at the point of the drill. In this case the burr will be shaped like a flower and will be very large. Figure 7 illustrates the types of burrs discussed. Type A and type B burrs are easily measured with the proper equipment, while type C burrs are very difficult to measure due to their shape.

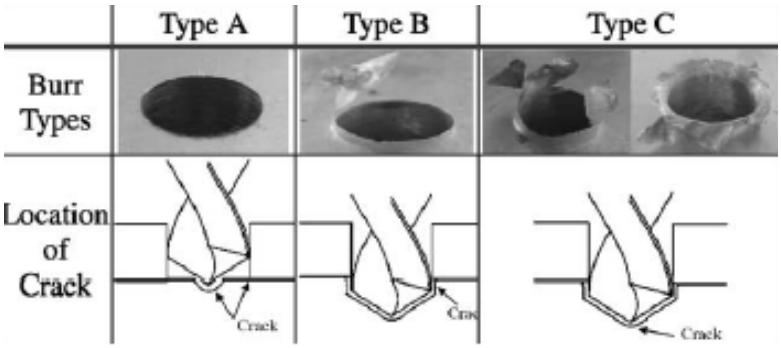

Figure 7: Burr Types as Defined by Ko et al. [15]

2.4.2 Burr Characterization

Burr measurement style and characterization depends on the researcher and the available equipment. When there is a wide variation in burr height and the height is reasonably large, burrs can be measured using an optical comparator [7]. In other works where there is a smaller variation in burr height, it can be measured using a tool-maker's microscope. Burr size can also be characterized in a few ways. Some studies only report the burr height, while others also measure the burr thickness [16]. Burr height is measured in this work. Once burrs are characterized and measured they can then be studied and modeled, which will be reviewed in the following section.

2.4.3 Modeling Burr Formation

Many researchers have studied burr formation in drilling using an empirical or finite element approach. Ramu et al. [23] created empirical models for thrust, torque and burr height when drilling mild steels concluding that burr height is minimized by minimizing thrust and maximizing torque. Pande and Relekar [21] used response surface methodology (RSM) to correlate the burr size to experimental parameters including feed, hole size and workpiece hardness and developed a system to continuously adjust the feed throughout the drilling process in order to reduce burrs. In RSM relationships are developed between inputs (such as feed, speed, drill geometry) and outputs (burr size) that are either linear, polynomial or 2-factor interactions which are then

plotted for analysis [11]. Response surface methodology was also used in addition to genetic algorithm to minimize burr height [5] [12]. Genetic algorithm is an optimization method based on the principle of natural selection. There are many different types of empirical methods such as RSM or artificial neural networks (ANN) and optimization tools such as genetic algorithm and particle swarm optimization (PSO) that are used to minimize burr heights, but these methods are based on regression to determine the relationships between input parameters, not on the kinematics of the process. Finite element approaches have been used by many researchers such as Kim and Dornfeld [13], Min et al. [19] and Isbilir and Ghassemieh [8], using simulation software to model burr formation and experiments to validate their results.

2.5 Summary

Thrust and torque models in drilling have been developed by many researchers using empirical, mechanistic or finite element approaches. The empirical approach requires more experiments to calibrate and regression models are used to determine the relationships between input parameters and outputs while the mechanistic approach is based on the kinematics of the process and requires fewer experiments to calibrate. The finite element approach is simulation-based and experiments are only necessary for validation. Because of these differences the mechanistic modeling approach is used in this thesis, combining experimental and modeling work while reducing calculation time. Burrs are also investigated later in this thesis and they are characterized by burr height. Following the results of prior work this investigation will focus on burr heights produced when drilling with standard twist drills and with step drills without a split point.

CHAPTER III

DRILLING FORCE MODEL

In this chapter a mechanistic force model is developed to predict the thrust and torque produced in drilling. The formulation of this mechanistic model requires knowledge of the physics of the process, including how different variables interact. The following sections describe the material removal mechanisms occurring on the cutting lips and chisel edge of a standard twist drill. While the cutting lips remove material by oblique cutting, the chisel edge uses two different mechanisms. At the very center of the chisel edge the drill acts as an indenting wedge and at the outer section of the chisel edge orthogonal cutting occurs [20]. The basis of this model was developed by Chandrasekharan [2] but in this work a new way to model the orthogonal cutting mechanism occurring on the chisel edge is introduced. A modified version of this model is also introduced to predict thrust and torque for a step drill.

3.1 Basic Approach

In the formulation of a mechanistic model the geometry and kinematics of the process are modeled explicitly while calibration constants are used to model the material characteristics, such as the material strength. In this application the geometry of a twist drill and experimental conditions, such as speed and feed, are input directly into the model while the yield shear stress and other material properties are indirectly included in the model through the calibration constants.

The cutting forces in this model are described as functions of the normalized radial coordinate (ρ), which is defined as the ratio between the instantaneous radius (r) and the drill radius (R) as given in Equation 4. Figure 8 illustrates these parameters while also identifying the different cutting sections of the drill including the cutting lips and

chisel edge, which is the combination of secondary cutting edges and the indentation zone.

$$\rho = r/R \tag{4}$$

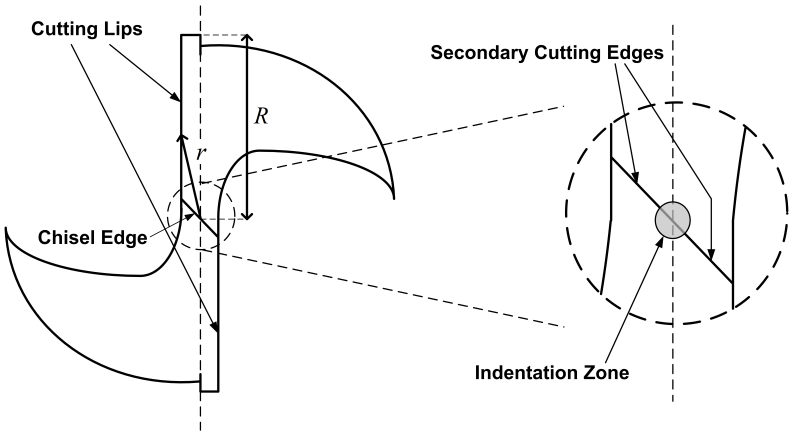

Figure 8: Twist Drill Cutting Sections

This model is developed in terms of the normalized radial coordinate to enable the model to be easily used for drills of different diameters but similar geometries. The following sections reexamine the mechanistic model developed by Chandrasekharan [2] for the cutting lips and chisel edge of a twist drill. In Section 3.2 the oblique cutting model is developed for the cutting lips. It is followed by model development for the chisel edge in Section 3.3, including an orthogonal model for the secondary cutting zone and the indentation zone model.

3.2 Primary Cutting Zone - Cutting Lips

The cutting lips of a drill remove material by means of oblique cutting. The chisel edge of a drill gives the point stability and reduces drill wandering. It also causes the cutting lips to be off-center but parallel to a plane containing the axis of the drill as shown in Figure 9.

The resulting force acting on a rotating drill can be resolved into its normal,

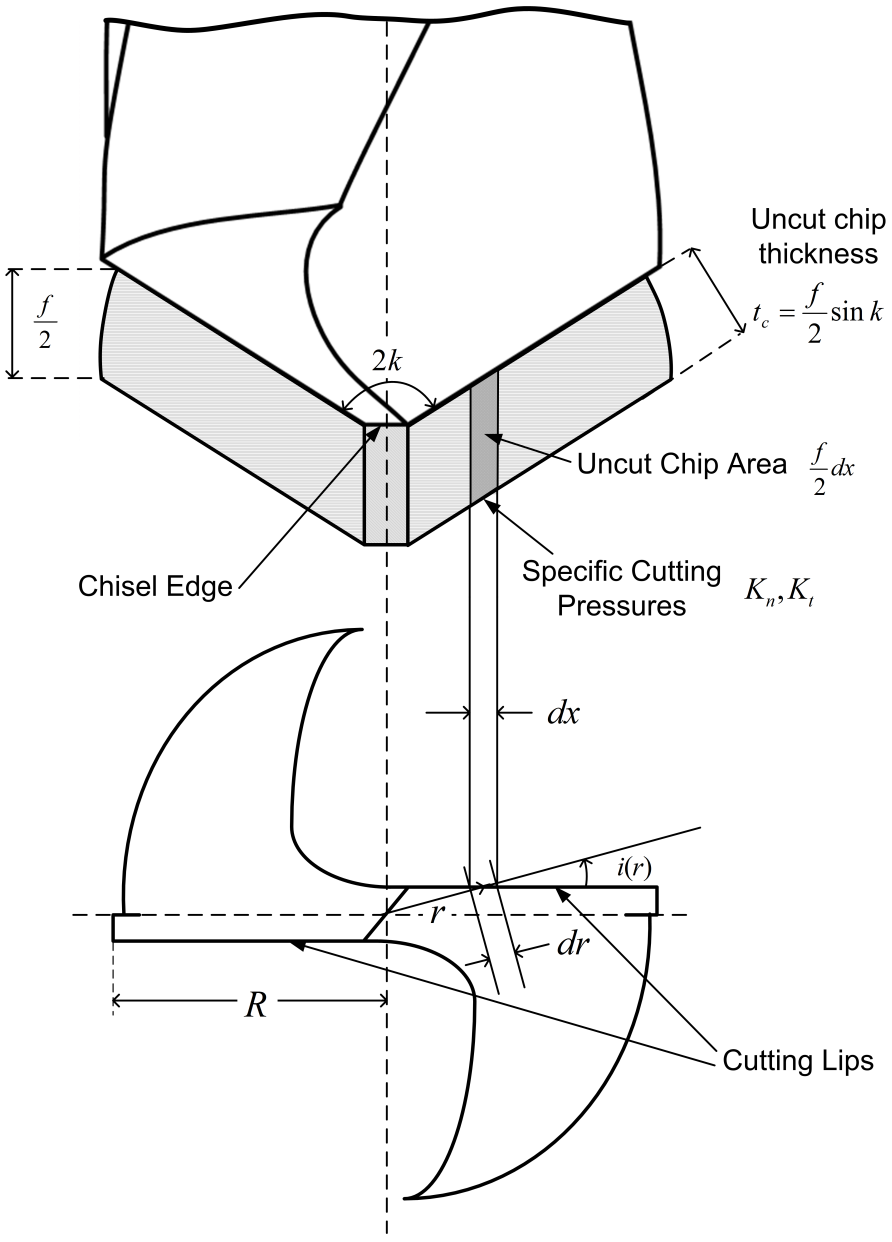

Figure 9: Drill Pressure Areas {adapted from [2]}

tangential and radial components as shown in Figure 10. It is assumed that the cutting lips can be divided into segments also known as elements. The elemental cutting forces in the normal (dF_n) and tangential (dF_t) directions acting on each segment are computed by multiplying the specific cutting pressures in the normal (K_n) and tangential (K_t) directions by the uncut chip area defined by $\frac{f}{2}\,dx$ described in Equations 5 and 6.

$$dF_n(\rho) = K_n(\rho)\,\frac{f}{2}\,dx = K_n(\rho)\,\frac{f}{2}\,cos\,i(\rho)\,R\,d\rho \tag{5}$$

$$dF_t(\rho) = K_t(\rho)\,\frac{f}{2}\,dx = K_t(\rho)\,\frac{f}{2}\,cos\,i(\rho)\,R\,d\rho \tag{6}$$

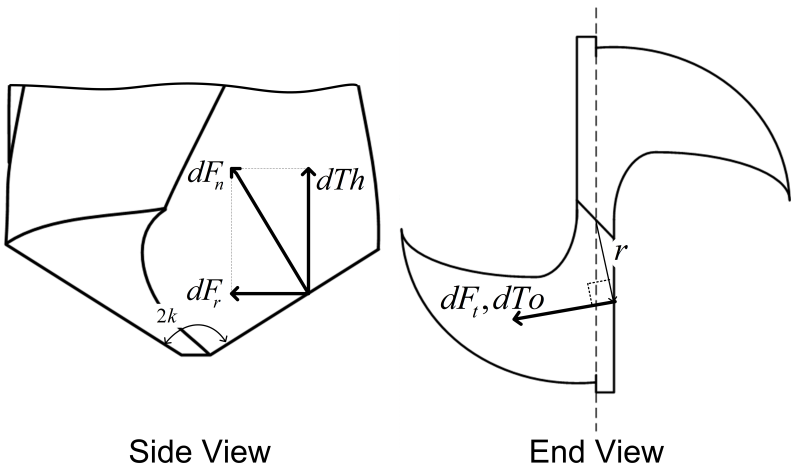

Figure 10: Elemental Drill Forces {adapted from [2]}

The chip width (dx) in Equations 5 and 6 is measured along the projection of the cutting lips onto a plane perpendicular to the axis of the drill. It is also described according to the normalized radial coordinate using the inclination angle ($i(\rho)$) as shown in Equation 7.

$$dx = cos\,i(\rho)\,R\,d\rho \tag{7}$$

The normal and tangential forces are transformed into thrust and torque for calibration and validation purposes because normal and tangential forces are not measured directly by a dynamometer. This transformation is performed on the drill geometry resulting in the relationships presented in Equations 8 and 9, also shown in Figure 10.

$$Th_{CL} = F_n \, sin\,(k) = \int_{\tau}^{1} 2\, dF_n(\rho)\, sin\,(k) = \int_{\tau}^{1} 2\, K_n(\rho)\, \frac{f}{2}\, sin\,(k)\, cos\, i(\rho)\, R\, d\rho \quad (8)$$

$$To_{CL} = \int_{\tau}^{1} 2\, F_t(\rho)\, R\, d\rho = \int_{\tau}^{1} 2\, K_t(\rho)\, \frac{f}{2}\, R^2 \rho\, cos\, i(\rho)\, d\rho \quad (9)$$

The endpoints of the integration (τ,1) in Equations 8 and 9 give the range of radial coordinate values along the cutting lips. Tau (τ) is the value of the normalized radial coordinate at the intersection of the chisel edge and cutting lips, calculated using Equation 10. The components of Equation 10 are illustrated in Figure 3 in Section 2.1.

$$\tau = \frac{web\, length}{D} = \frac{2w}{\cos(\psi - 90^{\circ})\, D} \quad (10)$$

The uncut chip thickness (t_c) remains constant along the cutting lips (see Figure 9). It has been experimentally shown that the relationship between the specific cutting pressures and the uncut chip thickness, and tangential velocity is best described by the power law when different feeds are considered [2] [24]. These findings lead to expressions for the specific cutting pressures described in Equations 11 and 12 [2].

$$K_n = a_0\, t_c^{a_1}\, V^{a_2}\, e^{a_3 \alpha_n} \quad (11)$$

$$K_t = b_0\, t_c^{b_1}\, V^{b_2}\, e^{b_3 \alpha_n} \quad (12)$$

The normal rake angle (α_n) is the angle between the workpiece and the cutting face of the drill. It is not constant along the cutting lips of the drill, it varies with instantaneous radial value as defined in Equation 3 in Section 2.1. Equations 11 and

12 can be combined with Equations 8 and 9 to give the equations for total drilling thrust and torque as shown in Equations 13 and 14.

$$Th_{CL} = \int_{\tau}^{1} a_0 \, t_c^{a_1} \, V^{a_2} \, e^{a_3 \alpha_n} \, f \, sin\,(k) \, cos\, i(\rho) \, R \, d\rho \tag{13}$$

$$To_{CL} = \int_{\tau}^{1} b_0 \, t_c^{b_1} \, V^{b_2} \, e^{b_3 \alpha_n} \, f \, R^2 \rho \, cos\, i(\rho) \, d\rho \tag{14}$$

The uncut chip thickness (t_c), cutting velocity (V) and normal rake angle (α_n) are all functions of the radial coordinate (ρ). In order to solve for the calibration constants connected to these components ($a_0, a_1, a_2, a_3, b_0, b_1, b_2, b_3$) the equations for the specific cutting pressures must be developed such that the thrust and torque equations can be integrated. Because the uncut chip thickness, tangential velocity and normal rake angle all depend on ρ, Equations 13 and 14 become complex to evaluate. To solve this problem, the specific cutting pressures are determined directly as functions of the radial coordinate before solving for the four constants in each equation. The theory of geometrically similar drills is used for this transformation. Two drills are considered geometrically similar if they meet the following criteria.

- Same point angle ($2k$)
- Same helix angle (α_{hxo})
- Same value of τ
- Ratio of their diameters is equal to the inverse of the ratio of their spindle speeds

$$\frac{D_1}{D_2} = \frac{N_2}{N_1}$$

Geometrically similar drills will have the same tangential velocity at a particular value of ρ. They will have the same uncut chip thickness if they have the same feed (in/min). Due to geometric similarity, simplified equations are used to express the

specific cutting pressures depending only on the normalized radial coordinate and two calibration constants for each of thrust and torque as shown in Equations 15 and 16.

$$K_n = C_1\,\rho^a \tag{15}$$

$$K_t = C_2\,\rho^b \tag{16}$$

Using the simplified equations for the specific cutting pressures, solutions of the thrust and torque can be calculated, making calibration possible using Equations 17 and 18.

$$Th_{CL} = \int_{\tau}^{1} C_1\,\rho^a\; f\; sin\,(k)\; cos\, i(\rho)\; R\, d\rho \tag{17}$$

$$To_{CL} = \int_{\tau}^{1} C_2\,\rho^b\; f\; R^2\rho\, cos\, i(\rho)\, d\rho \tag{18}$$

When determining the solutions of Equations 17 and 18 an approximation of the cosine of the inclination angle is used as displayed in Equation 19.

$$\begin{aligned} cos\, i(\rho) &= cos\,\left(sin^{-1}\left(\frac{w}{R\,\rho} sin\, k\right)\right) = \left\{1 - sin^2 i(\rho)\right\}^{1/2} \\ &= \left\{1 - \left(\frac{w}{R\,\rho} sin\, k\right)^2\right\}^{1/2} \cong \left\{1 - \frac{1}{2}\frac{w^2 sin^2 k}{R^2\rho^2}\right\} \end{aligned} \tag{19}$$

This simplification results in the closed-form solutions for thrust and torque as shown in Equations 20 and 21.

$$Th_{cl} = \frac{C_1\, R\, f\; sin\, k}{a+1}\left\{1 - \tau^{(a+1)}\right\} - \frac{C_1\, f\, w^2 sin^3\, k}{2R(a-1)}\left\{1 - \tau^{(a-1)}\right\} \tag{20}$$

$$To_{cl} = \frac{C_2\, R^2\, f}{b+2}\left\{1 - \tau^{(b+2)}\right\} - \frac{C_2\, f\, w^2 sin^2\, k}{2b}\left\{1 - \tau^{b}\right\} \tag{21}$$

With these closed-form solutions for the thrust and torque, the cutting lips model can be calibrated and the thrust and torque for untested parameters can be predicted. The following section develops the the mechanistic model for the chisel edge of a twist drill.

3.3 Chisel Edge

Two different types of material removal occur on the chisel edge when drilling metals [20]. Orthogonal cutting occurs outside of a critical radius (R_a) in the secondary cutting zone similar to the cutting lips. At the very center of the drill, inside the critical radius, the chisel edge acts as an indenting wedge. In the next section the mechanistic model is developed for the secondary cutting zone.

3.3.1 Secondary Cutting Zone

In previous research [2] the solution to the cutting lips model was extrapolated onto the secondary cutting zone assuming that the relationship between the tangential velocity, uncut chip thickness and normal rake angle and the thrust and torque does not change. On the chisel edge the tangential velocity is smaller, the normal rake angle becomes constant, while it varies on the cutting lips, and the uncut chip thickness is not dependent on the point angle because the chisel edge is assumed to lie in a plane perpendicular to the axis of the drill, resulting in a point angle of zero. Because of these differences an orthogonal model for calculating the thrust and torque in the secondary cutting zone is formulated. This orthogonal model has the same basis as the oblique model used on the cutting lips with the few differences mentioned above. Also, the cutting edge intersects the axis of the drill resulting in zero inclination angle on the chisel edge. The constant value of the normal rake angle is defined by Equation 22 [18].

$$\alpha_{n,ch} = -tan^{-1}\{tan\, k\, cos\, (\pi - \psi)\} \tag{22}$$

The chisel edge angle (ψ) is defined as the angle between the cutting lip and chisel edge, measured in a plane perpendicular to the axis of the drill (Figure 3). Equations 8 and 9 from the cutting lips are adapted to the secondary cutting zone on the chisel edge in Equations 23 and 24.

$$Th_{scz} = \int_{\rho_a}^{\tau} K_{n,ce}(\rho)\, f\, R\, d\rho \tag{23}$$

$$To_{scz} = \int_{\rho_a}^{\tau} K_{t,ce}(\rho)\, f\, R^2\, \rho\, d\rho \tag{24}$$

The thrust and torque equations for the secondary cutting zone are integrated from the normalized radial value of the indentation zone (ρ_a) up to the intersection between the chisel edge and the cutting lips at a normalized radial value of τ.

Previous authors working with a mechanistic model for drilling have taken the calibration constants on the cutting lips and extended their use onto the secondary cutting zone [2]. This involves extrapolating from a region of positive rake angles to a region with a constant negative rake angle which is a limitation of the formulation. To address this issue, in this thesis the secondary cutting zone is calculated separately from the cutting lips. The specific cutting pressures are defined in the same way as on the cutting lips (Equations 11 and 12), but because the normal rake angle is a constant on the chisel edge a simplification is made to the specific cutting pressures as shown in Equations 25 and 26.

$$K_{n,ce} = a_0\, t_c^{a_1}\, V^{a_2}\, e^{a_3 \alpha_n} = a_4\, t_c^{a_1}\, V^{a_2} \tag{25}$$

$$K_{t,ce} = b_0\, t_c^{b_1}\, V^{b_2}\, e^{b_3 \alpha_n} = b_4\, t_c^{b_1}\, V^{b_2} \tag{26}$$

By combining $a_0\, e^{a_3 \alpha_n}$ into a_4 and $b_0\, e^{b_3 \alpha_n}$ into b_4 the number of calibration steps necessary is reduced, while improving the precision of the model over the original extrapolated model. Because the chisel edge of a drill is virtually flat, it is extremely difficult to gather force data as the drill is entering the workpiece and distinguish the thrust and torque associated with particular radial values. To calibrate thrust and torque on the chisel edge, drilling tests were performed with pilot holes of different sizes ranging from the size of the indentation zone to the web length as discussed in the next chapter.

3.3.2 Indentation Zone

In prior work, a geometric analysis was performed to locate and provide an expression for the radius of the indentation zone [18] resulting in Equation 27.

$$R_a = \frac{f}{2\,tan\,(\frac{\pi}{2} - k)} \tag{27}$$

The thrust and torque due to indentation within this region are calculated using a slip line field analysis developed by Kachanov [9] for an indenting wedge resulting in Equations 28 and 29.

$$Th_{ind} = \frac{4\,K\,(1+\varepsilon)\,f\,R_a\,sin\,\alpha_{n,ch}}{cos\,\alpha_{n,ch} - sin(\alpha_{n,ch} - \varepsilon)} \tag{28}$$

$$To_{ind} = \frac{2\,K\,(1+\varepsilon)\,f\,R_a^2\,cos\,\alpha_{n,ch}}{cos\,\alpha_{n,ch} - sin(\alpha_{n,ch} - \varepsilon)} \tag{29}$$

The following assumptions are made in this model,

- The workpiece is a semi-infinite plastic-rigid medium
- The wedge is rigid and symmetric
- Friction at the contact surface is neglected.

Although there is friction at the surface, the model is a good approximation of the indenting process at the center of the chisel edge. Epsilon (ε) is the angle of the central field ADE shown in Figure 11. Epsilon (ε) is calculated in Equation 30 which cannot be solved directly but must be solved through an iterative process [9].

$$2\,|\alpha_{n,ch}| = \varepsilon + cos^{-1}\left\{tan\left(\frac{\pi}{4} - \frac{\varepsilon}{2}\right)\right\} \tag{30}$$

The yield shear stress of the workpiece is denoted by K. The theoretical value for the yield shear stress is not used to solve for the thrust and torque in the indentation zone because it does not account for strain hardening, temperature distribution and

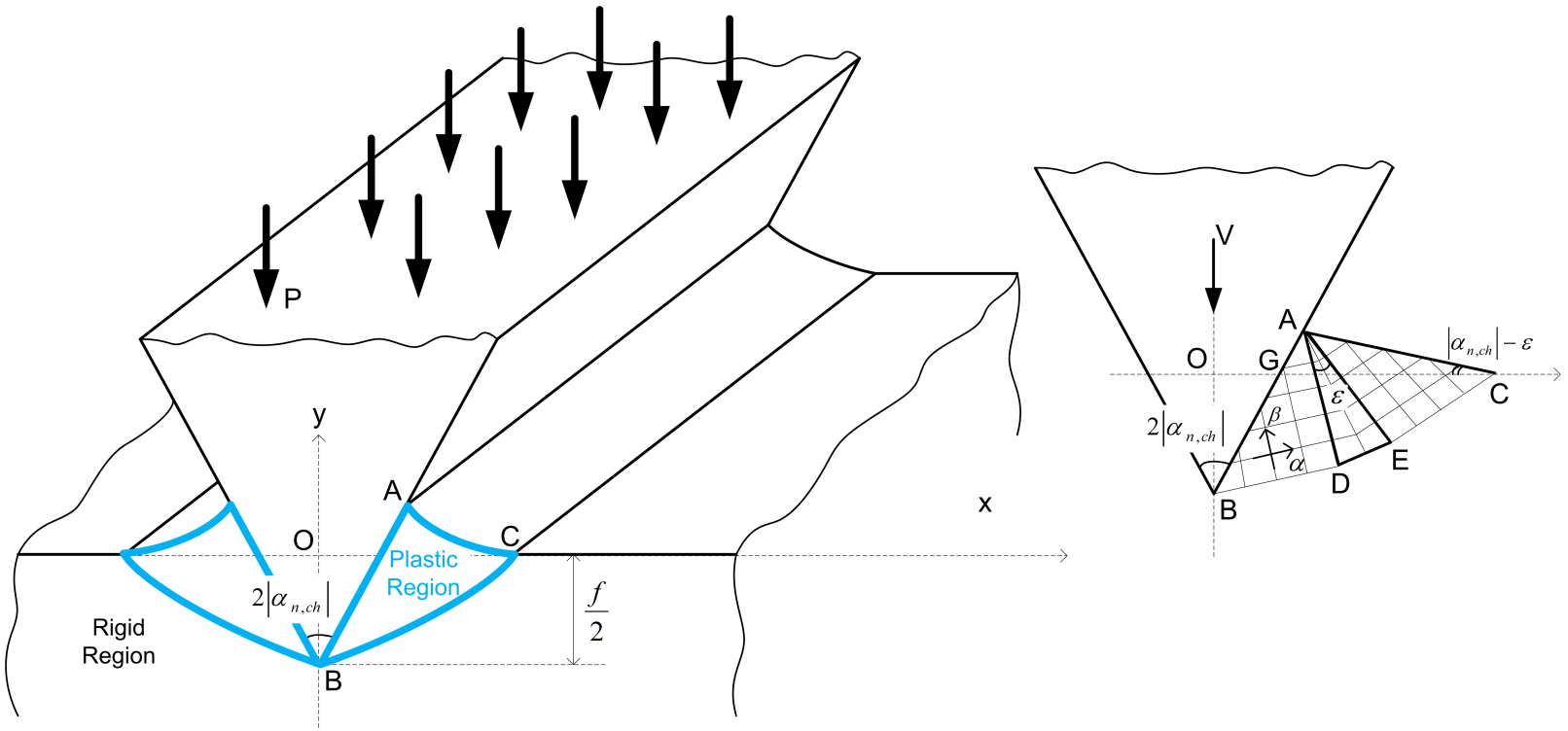

Figure 11: Indentation Zone. Adapted from [9]

strain rate effects. It is calculated by subtracting the cutting lips thrust and secondary cutting zone thrust from the total thrust in calibration tests and solving for K from the thrust equation for the indentation zone as shown in Equations 31 and 32. Because the torque due to the chisel edge is very low, using the thrust is preferred as it is less likely to be susceptible to experimental errors [2].

$$Th_{ind,K_{calc}} = Th_{total} - Th_{cl} - Th_{scz} \tag{31}$$

$$K_{calc} = \frac{Th_{ind,K_{calc}} \cos \alpha_{n,ch} - sin(\alpha_{n,ch} - \varepsilon)}{4\,(1+\varepsilon)\,f\,R_a\,sin\,\alpha_{n,ch}} \tag{32}$$

3.4 Complete Model

Once the formulation and calibration of the model has been completed, the thrust and torque models can be displayed graphically as shown in Figures 12 and 13.

In section 1 in the figures, the drill is entering a workpiece with a pilot hole the size of the chisel edge so only the cutting lips are drilling. The drill is fully engaged within the pilot hole in section 2. In section 3, the drill has reached the end of the pilot hole and the chisel edge is engaged as well as the cutting lips, giving the total thrust and torque for the drill. Equations 33 and 34 give the components of the thrust and torque.

$$Th_{total} = Th_{ind} + Th_{scz} + Th_{cl} \tag{33}$$

$$To_{total} = To_{ind} + To_{scz} + To_{cl} \tag{34}$$

3.5 Step Drill Model

This mechanistic model can be adapted for use with a step drill. The model is formulated in a similar way to the standard twist drill except a second point angle is added to the drill, called the secondary point angle or step angle. The chisel edge model, including the indentation zone and secondary cutting zone will not change for modeling a step drill. The model of the cutting lips will change because they will be

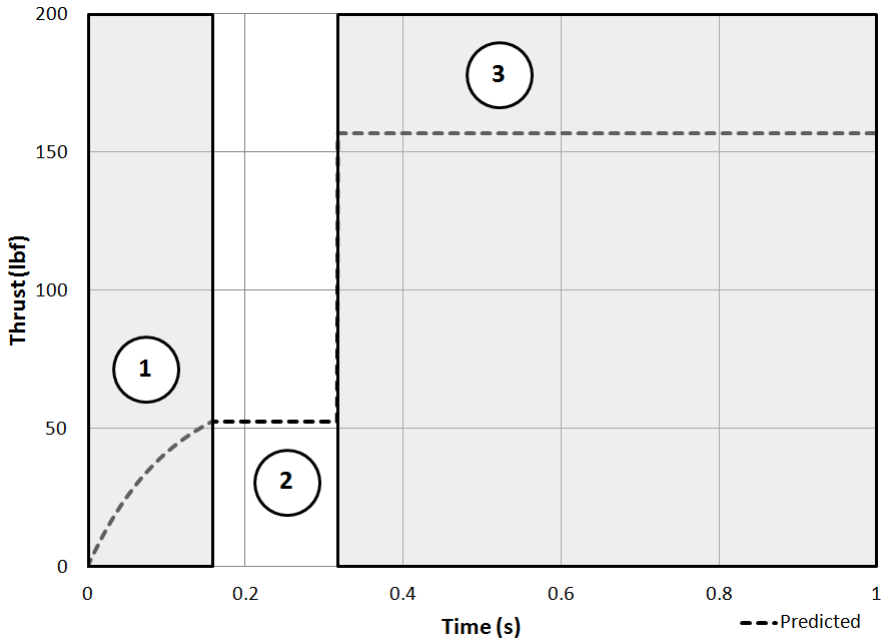

Figure 12: Thrust Model: Speed 6000 rpm, Feed 0.006 ipr

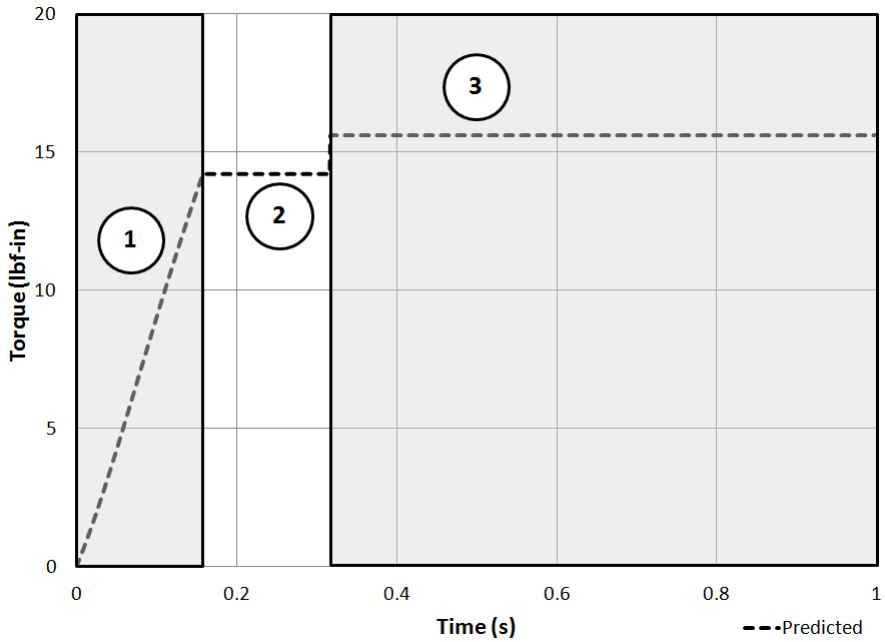

Figure 13: Torque Model: Speed 6000 rpm, Feed 0.006 ipr

divided into two separate sections. The cutting lips on the primary point will cut in the same fashion as described in previous sections. It is assumed that the thrust and torque applied by the step length located between the primary and secondary points is negligible. Then the cutting lips of the secondary point will cut similarly to the primary point cutting lips, except there will be a different point angle. Equations 35 and 36 give the components of the thrust and torque when using a step drill, which can be compared to Equations 33 and 34 for a twist drill without a step.

$$Th_{total,step} = Th_{ind} + Th_{scz} + Th_{cl,primary} + Th_{cl,secondary} \tag{35}$$

$$To_{total,step} = To_{ind} + To_{scz} + To_{cl,primary} + To_{cl,secondary} \tag{36}$$

Figures 14 and 15 display the predicted thrust and torque for the step drill. The model is formulated to predict the thrust and torque when drilling with a step drill without a pilot hole. In section 1, the chisel edge of the drill is engaging, including the indentation zone and the secondary cutting zone. Section 2 displays the forces resulting from the primary point angle up to the inner diameter. In section 3 the step length is engaging and the additional thrust and torque due to this region is assumed to be negligible. In the fourth section the step angle is engaging and in section 5 the drill is fully engaged.

3.6 Summary

The mechanistic model for thrust and torque produced in drilling is developed in this chapter. The point of the drill is separated into three sections, each of which is modeled separately. The cutting lips are modeled using an oblique cutting model while the secondary cutting zone uses an orthogonal model because there is no inclination angle or point angle along the chisel edge. The center of the chisel edge is modeled as an indenting wedge using the slip line field analysis developed by Kachanov [9]. The total thrust and torque produced by a standard twist drill is calculated to be the sum

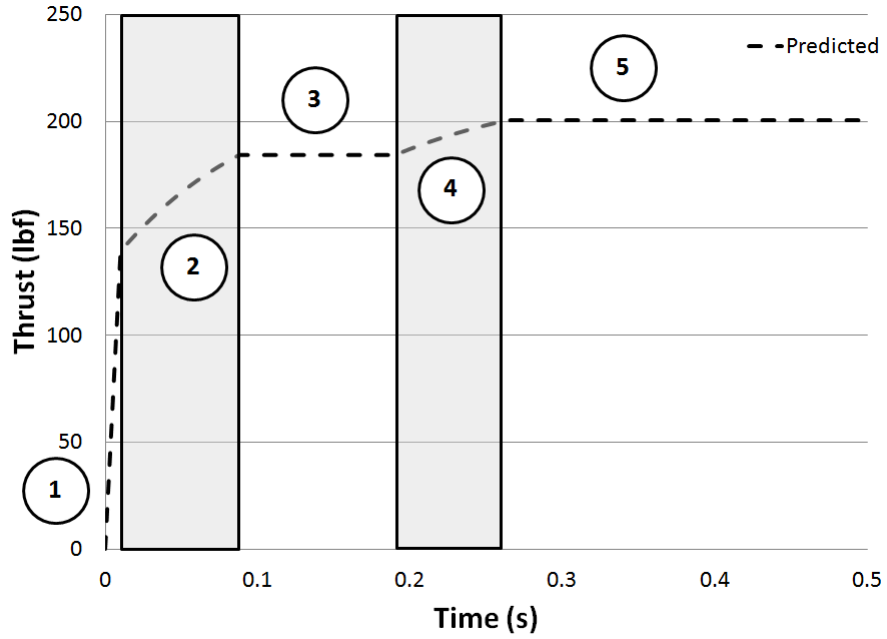

Figure 14: Step Drill Thrust Model: Speed 4500 rpm, Feed 0.009 ipr, Inner Diameter 0.2 in, Secondary Point Angle 100 deg

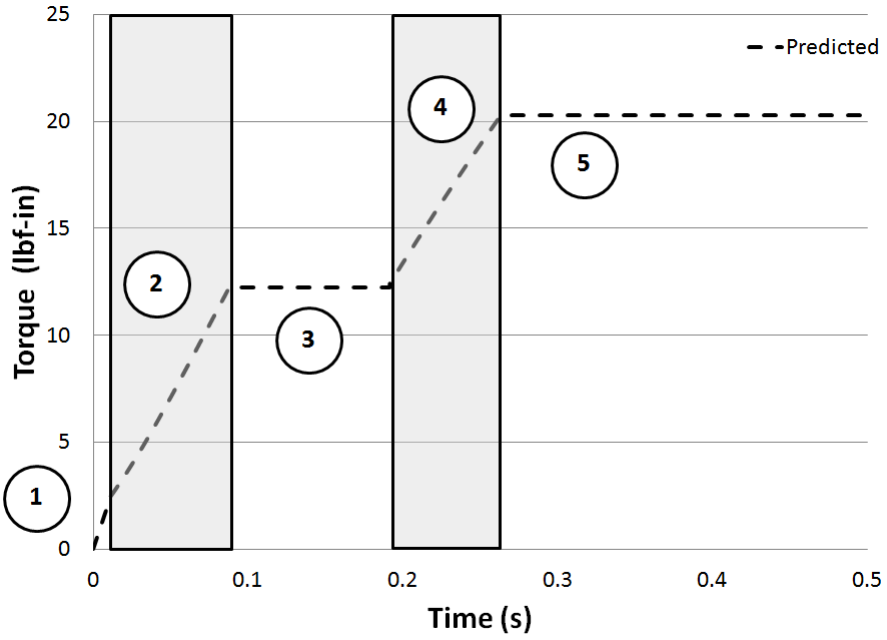

Figure 15: Step Drill Torque Model: Speed 4500 rpm, Feed 0.009 ipr, Inner Diameter 0.2 in, Secondary Point Angle 100 deg

of the components from each of these three sections. Once the model is calibrated and validated, it is further modified to predict the thrust and torque produced by a step drill. This is done by the addition of a cutting lips section that is modeled between the inner diameter and drill diameter with a secondary point angle which differs from the primary point angle. The following chapter discusses the calibration and validation procedures for the standard and step drills.

CHAPTER IV

FORCE MODEL CALIBRATION AND VALIDATION

This chapter gives the process by which the thrust and torque models are calibrated and validated. Experiments are performed to calibrate the cutting lips first, followed by the secondary cutting zone and indentation zone on the chisel edge. Similar procedures are used for the cutting lips and chisel edge calibrations, using blind pilot holes of different diameters to isolate sections of interest of the drill point. In the following sections the experimental setup and testing will be described followed by the procedure used for calibration and validation of the force model for each section of the drill.

4.1 Cutting Lips Calibration

Experiments are performed in order to calibrate the thrust and torque models shown in Equations 20 and 21. The experimental data is used to calculate the C_1, a, C_2, b values and then the specific cutting pressure equations (Equations 11 and 15 in the normal direction and Equations 12 and 16 in the tangential direction) are set equal to one another to solve for the full set of calibration constants $(a_0, a_1, a_2, a_3, b_0, b_1, b_2, b_3)$.

4.1.1 Experimental Setup and Testing

High speed steel jobber drills manufactured by Hertel were acquired for experimental testing, as well as Al7075-T651 to be used as the workpiece material. To verify the point angle and diameter of the drills a small sample of blind holes were drilled into workpiece material and the geometry produced in the workpiece was measured using a LEXT 3D laser confocal microscope. The chisel edge angle, web length and helix angle were measured directly from a sample drill because the manufacturer was unable

to provide specifications for the drill. The chisel edge measurement is shown in Figure 16. The nominal and measured values of the drill geometry are given in Table 1.

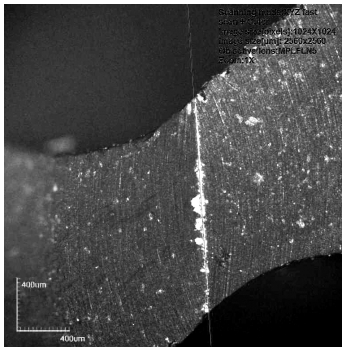

Figure 16: Chisel Edge Length Measured on the Confocal Microscope

Table 1: Drill Geometry Measurements

	Nominal	**Measured**
Diameter (D) (in)	0.3125	0.3156 ± 0.0017
Point angle ($2k$) (degrees)	118	110 ± 1
Chisel edge angle (ψ) (degrees)	-	130 ± 2
Web length (in)	-	0.063 ± 0.002
Helix angle (α_{hxo}) (degrees)	-	30 ± 2

The measured geometry was used in calibration and validation of the force model. This was done so that the most accurate values were used. By using the measured value of the diameter of the hole any runout of the spindle is accounted for in the geometry and does not need to be considered at another point in the model. By using the measured point angle, it is verified that the geometry used in the model is the geometry that the workpiece sees.

The experimental setup for calibration and validation is shown in Figure 17. Tests were performed using an Okuma MILLAC44V 3-axis CNC mill. During experiments,

data was acquired using a Kistler Type 9272 quartz 4-component dynamometer connected to a Kistler dual mode amplifier, model 5010. The output signal was captured using LabVIEW Signal Express 2009. All post-processing was performed using Matlab R2010b. All experiments were performed dry, without coolant.

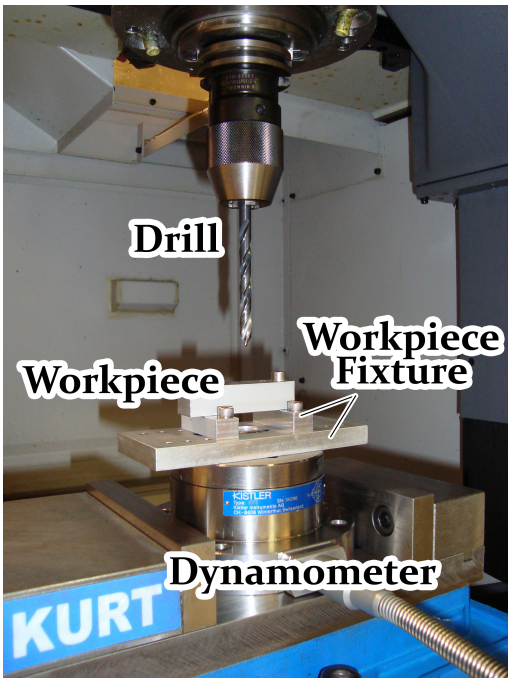

Figure 17: Experimental Setup for Calibration and Validation of Mechanistic Model

Three experiments are necessary to calibrate the cutting lips model. Two tests must be performed with the same feed, but different speeds (set A) and two tests must be performed with the same speed and different feeds (set B). One test can be used for both sets A and B, reducing the minimum number of experiments to three. To improve the accuracy of the calibration one test is added to each set so that fitting can be performed with three data points instead of two. The speeds and feeds for the calibration tests are shown in Table 2.

To make the model as accurate as possible, thrust and torque data is recorded as the drill enters the workpiece which is pre-drilled with a blind pilot hole equal in

Table 2: Calibration Tests

Set	Speed (rpm)	Feed (ipr)
A	3000	0.006
B	4500	0.004
A,B	4500	0.006
B	4500	0.009
A	6000	0.006

diameter to the web length for the cutting lips calibration. This pilot hole allows the forces from the chisel edge to be separated from the forces on the cutting lips. For the chisel edge calibration the diameter of the pilot hole ranges in size from the diameter of the indentation zone ($2R_a$) to the web length as shown in Figure 18. Data is recorded as the drill enters the workpiece. This records thrust and torque values for an almost infinite number of radii values, which is an advantage over running many tests with different pilot hole diameters. Performing multiple tests with different pilot hole diameters produces a less accurate fit of the model due to the reduction in data.

Figures 19 and 20 give the measured thrust and torque profiles, respectively, of the complete process. In region 1 of the figures, the drill is entering the workpiece where there is a pilot hole whose diameter is equal to the web length. In this region only the cutting lips are cutting. In section 2 the drill is fully engaged in the pilot hole. The drill exits the pilot hole and is fully engaged, cutting lips and chisel edge, in the workpiece in section 3.

4.1.2 Cutting Lips Model

The thrust and torque equations as a function of time (t) are given in Equations 37 and 38 and are used to solve for the calibration constants in the cutting lips model.

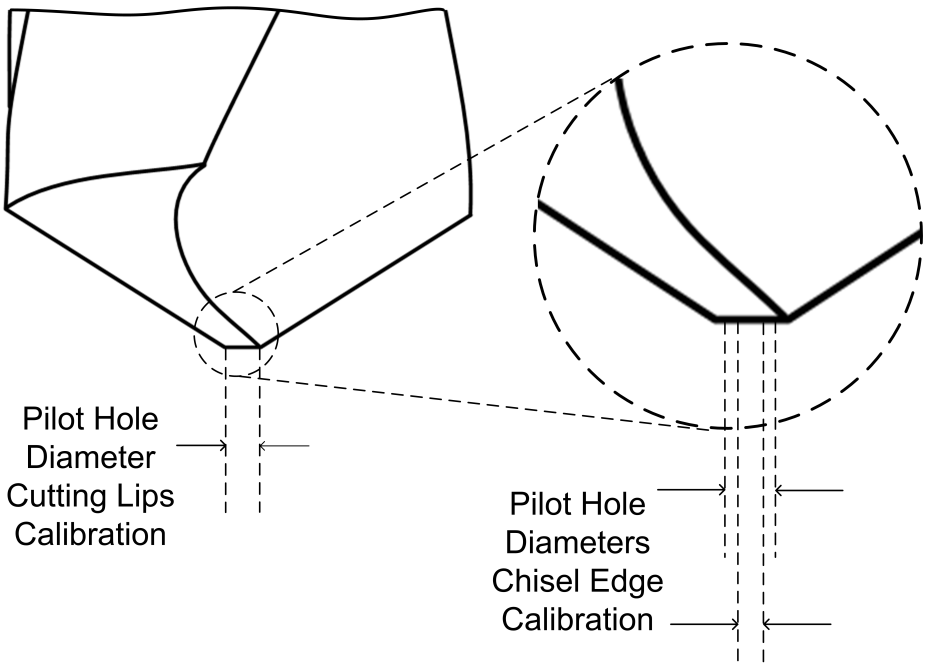

Figure 18: Pilot Holes for Cutting Lips and Chisel Edge Calibration

The radius of the pilot hole is designated as r_p.

$$Th_{cl}(t) = \frac{C_1\, R\, f\, sin\, k}{a+1}\left\{\left(\frac{r(t)}{R}\right)^{(a+1)} - \left(\frac{r_p}{R}\right)^{(a+1)}\right\} - \frac{C_1\, f\, w^2\, sin^3\, k}{2\, R\, (a-1)}\left\{\left(\frac{r(t)}{R}\right)^{(a-1)} - \left(\frac{r_p}{R}\right)^{(a-1)}\right\} \tag{37}$$

$$To_{cl}(t) = \frac{C_2\, R^2\, f}{b+2}\left\{\left(\frac{r(t)}{R}\right)^{(b+2)} - \left(\frac{r_p}{R}\right)^{(b+2)}\right\} - \frac{C_2\, f\, w^2\, sin^2\, k}{2\, b}\left\{\left(\frac{r(t)}{R}\right)^{b} - \left(\frac{r_p}{R}\right)^{b}\right\} \tag{38}$$

The instantaneous radius as a function of time ($r(t)$) is calculated using the feedrate (inches/second), time and the drill geometry as shown in Equations 39 and 40.

$$r(t) = \left\{\left(\frac{web\, length}{2}\right)^2 + \Delta^2 + 2\,\Delta\,\left[\left(\frac{web\, length}{2}\right)^2 - w^2\right]^{1/2}\right\}^{1/2} \tag{39}$$

$$\Delta = t\, f_{ips}\, tan\, k \tag{40}$$

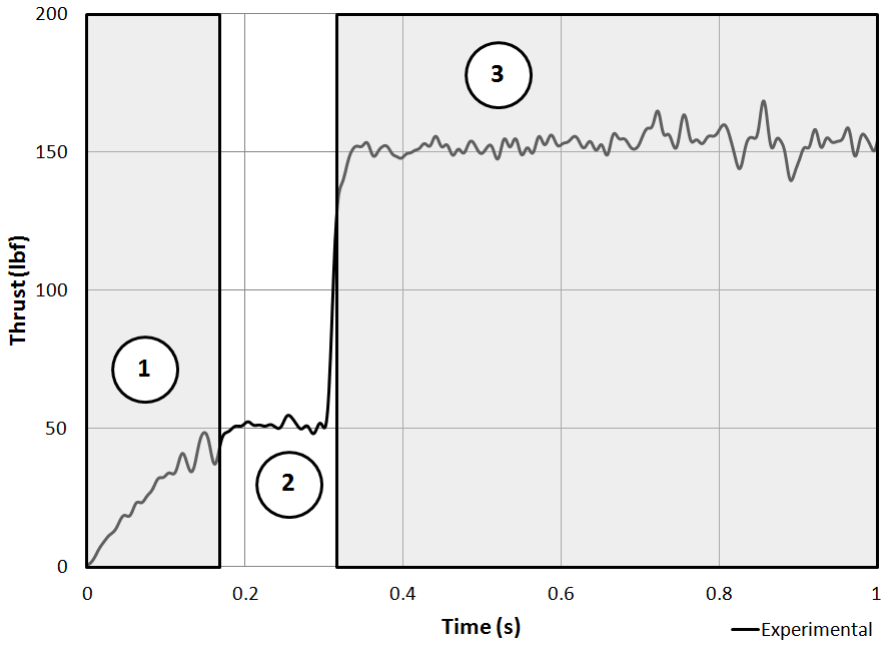

Figure 19: Measured Thrust: Speed 6000 rpm, Feed 0.006 ipr

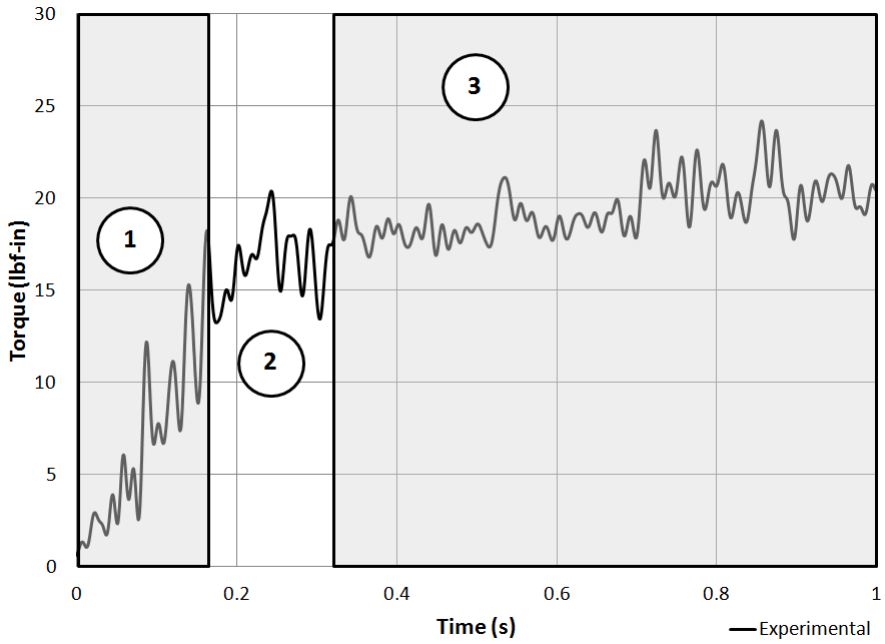

Figure 20: Measured Torque: Speed 6000 rpm, Feed 0.006 ipr

Equations 37 and 38 are solved for constants C_1, a, C_2, and b using the experimental data and Matlab software to perform a least-squares nonlinear fitting. The calculated constants are shown in Table 3. The average values of a and b are used to recalculate constants C_1 and C_2 for each test because it can be assumed that a and b depend only on the geometry of the drill, not on the experimental conditions [2]. Table 4 gives the recalculated values of C_1 and C_2.

Table 3: Calibration Constants: C_1, a, C_2, b

Speed (rpm)	**Feed (ipr)**	**Thrust (lbf)**	**Torque (lbf-in)**	$\mathbf{C_1}$	**a**	$\mathbf{C_2}$	**b**
3000	0.006	152.46	21.83	30285.75	-1.0952	112760.64	-0.9876
4500	0.004	125.99	12.87	35876.42	-1.1406	139932.42	-0.8508
4500	0.006	154.71	19.76	39896.34	-0.9457	122034.31	-0.9718
4500	0.009	195.80	26.10	36893.06	-0.7594	129849.27	-0.5148
6000	0.006	151.43	18.45	47167.69	-0.7591	102385.61	-1.1490
				average a	-0.9399	**average b**	-0.8948

Table 4: Recalculated Calibration Constants: C_1, C_2

Speed (rpm)	**Feed (ipr)**	$\mathbf{C_1}$	$\mathbf{C_2}$
3000	0.006	35123.8	121023.3
4500	0.004	43482.2	135380.9
4500	0.006	40102.5	128702.1
4500	0.009	31192.6	98513.2
6000	0.006	39866.7	124699.5

In order to calibrate the thrust and torque equations, the different derivations of the specific cutting pressures are set equal to one another (Equation 11 = Equation 15 and Equation 12 = Equation 16). Data from the three tests performed at the same speed with different feeds (set B) are used to calculate a_1 and b_1, the calibration

constants associated with the uncut chip thickness, as shown in Equations 41 and 42.

$$ln\, C_1 = ln\left[\frac{a_0\, V^{a_2}\, e^{a_3 \alpha_n}}{\rho^a}\right] + a_1\, ln\, t_c \tag{41}$$

$$ln\, C_2 = ln\left[\frac{b_0\, V^{b_2}\, e^{b_3 \alpha_n}}{\rho^b}\right] + b_1\, ln\, t_c \tag{42}$$

Because the three tests are performed at the same speed, the tangential velocities and normal rake angles are constant across the three tests. As a result, the middle components of Equations 41 and 42 are constant. After using the exponential function on the equation, a_1 and b_1 can be solved by using a least-squares fit. A similar procedure can be used to solve for a_2 and b_2 using data from the tests with the same feed and different speeds (set A) along with Equations 43 and 44.

$$ln\, C_1 = ln\left[\frac{a_0\, t_c^{a_1}\, (2\pi r)^{a_2}\, e^{a_3 \alpha_n}}{\rho^a}\right] + a_2\, ln\, N \tag{43}$$

$$ln\, C_2 = ln\left[\frac{b_0\, t_c^{b_1}\, (2\pi r)^{b_2}\, e^{b_3 \alpha_n}}{\rho^b}\right] + b_2\, ln\, N \tag{44}$$

Data from a single test can be used to solve for the remaining calibration constants (a_0, a_3, b_0, b_3) by rearranging the terms and using a least-squares fit. The test performed at 4500 rpm and 0.006 ipr was arbitrarily chosen, but the same constant values will result when using any of the five calibration experiments. The measured drill geometry shown in Table 1 resulted in the calibration constant values given in Equations 45 and 46 when drilling into a workpiece of Al7075-T651.

$$K_{n,cl} = 4586.59816\, t_c^{-0.40961598}\, V^{0.192197975}\, e^{-4.0170797\, \alpha_n} \tag{45}$$

$$K_{t,cl} = 38846.31956\, t_c^{-0.39202064}\, V^{0.05029512}\, e^{-3.48614065\, \alpha_n} \tag{46}$$

Using Equations 45 and 46 the experimental data can be compared to the model as shown in Figures 21 and 22.

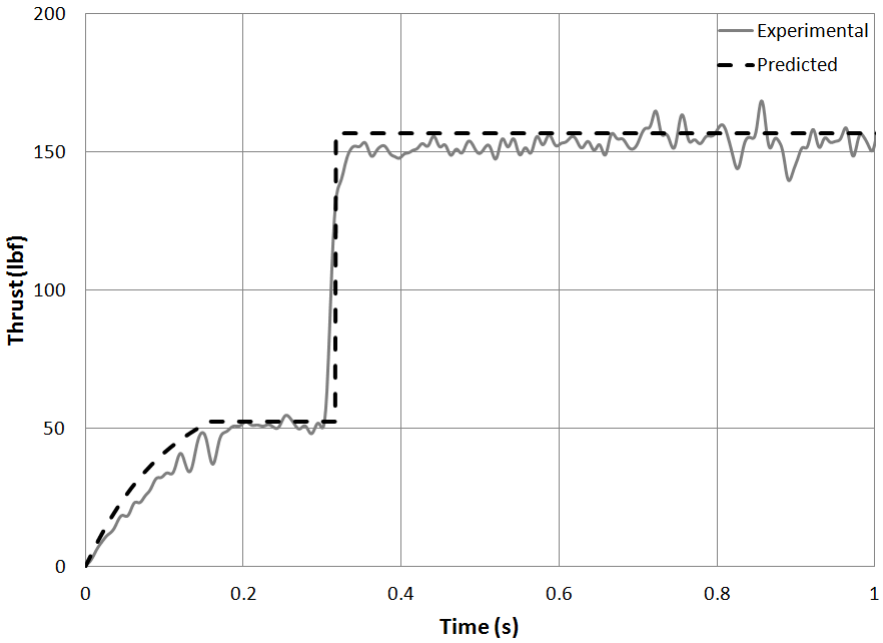

Figure 21: Measured and Predicted Thrust: Speed 6000 rpm, Feed 0.006 ipr

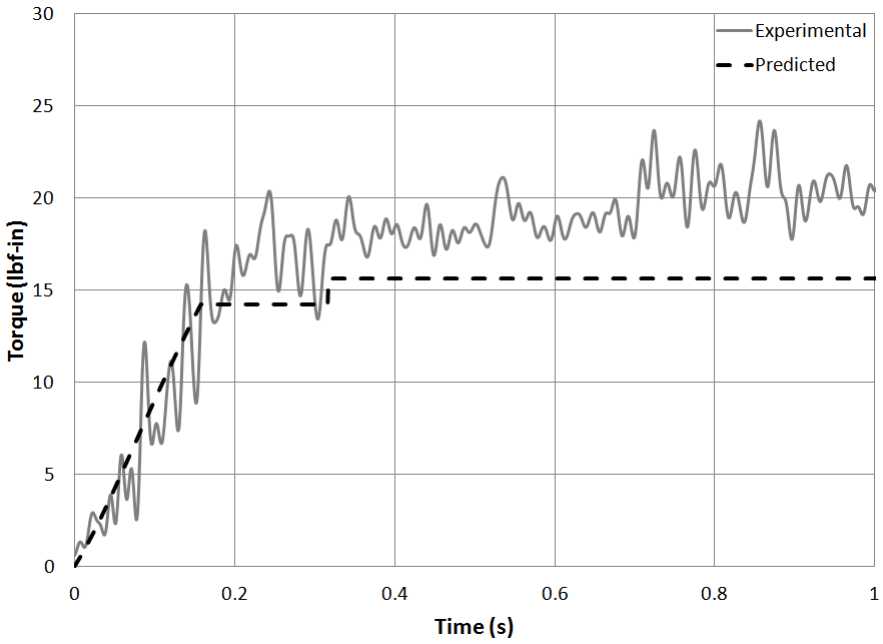

Figure 22: Measured and Predicted Torque: Speed 6000 rpm, Feed 0.006 ipr

4.2 Chisel Edge Calibration

The different cutting mechanisms on the chisel edge require different calibration procedures. At the center of the chisel edge, material is removed by indentation. Between a critical radius value (R_a) and the radius of the chisel edge orthogonal cutting occurs in the secondary cutting zone as shown in Figure 8. The processes used for calibrating the models for the secondary cutting zone and indentation zone are modified versions of that used on the cutting lips.

4.2.1 Secondary Cutting Zone

The chisel edge is assumed to be flat, making it difficult to use the same data collection method as used on the cutting lips. Five to seven tests are run at a given feed and speed with pilot hole radii ranging from the radius of the indentation zone to the radius of the chisel edge. The total thrust and torque due to the chisel edge within the pilot hole for each experiment is connected to the other pilot hole sizes for the same feed and speed to create one data set with the diameters of the pilot holes and the thrusts and torques within the pilot holes. The data sets for 4500 rpm and 0.009 ipr and for 3000 rpm and 0.006 ipr are given in Tables 5 and 6.

Table 5: Chisel Edge Calibration Data - 4500 rpm, 0.009 ipr

Pilot Hole Diameter (in)	**Thrust (lbf)**	**Torque (lbf-in)**
0.0149	13.21	4.46
0.0177	26.89	2.86
0.0225	32.50	2.92
0.0295	54.51	1.93
0.0400	88.60	4.65
0.0635	129.93	5.53

Because fewer data points are collected on the chisel edge, it is assumed that

Table 6: Chisel Edge Calibration Data - 3000 rpm, 0.006 ipr

Pilot Hole Diameter (in)	Thrust (lbf)	Torque (lbf-in)
0.0100	16.62	2.43
0.0125	24.04	3.67
0.0177	41.93	3.73
0.0225	46.33	1.86
0.0295	65.94	4.81
0.0400	71.91	5.87
0.0635	97.87	2.97

the model is not as accurate as the cutting lips model, but it is an improvement to extrapolating the cutting lips model to the chisel edge because the tangential speeds for the data within the chisel edge are used for calibration instead of the much higher tangential speeds on the cutting lips. The normal rake angle is also a constant and negative on the chisel edge and it is calibrated as such, which is different from the variable positive values for the chisel edge on the cutting lips. Solutions for the calibration constants C_1, a, C_2 and b obtained from Equations 17 and 18 in Chapter 3 and are shown in Table 7. As with the cutting lips, the average a and b values are used to recalculate the C_1 and C_2 values, which are shown in Table 8.

Table 7: Calibration Constants for the Secondary Cutting Zone: C_1, a, C_2, b

Speed (rpm)	Feed (ipr)	Thrust (lbf)	Torque (lbf-in)	C_1	a	C_2	b
3000	0.006	97.8744	2.9738	279683.4	-0.2359	7029.4	-1.8205
4500	0.004	83.8783	3.5651	702141.6	0.0073	83088.3	-1.2769
4500	0.006	93.4061	2.7504	525373.5	-0.0048	4863.7	-1.7958
4500	0.009	129.9250	5.5292	845769.9	0.2345	16870.0	-1.6073
6000	0.006	85.2462	2.6572	878451.3	0.2357	11141.7	-1.6800
				average a	0.0474	**average b**	-1.6361

From the calculated values of C_1, a, C_2, and b the full set of calibration constants

Table 8: Recalculated Calibration Constants for the Secondary Cutting Zone: C_1, C_2

Speed (rpm)	Feed (ipr)	C_1	C_2
3000	0.006	669298.0	22024.4
4500	0.004	786845.9	19256.8
4500	0.006	611912.8	12638.2
4500	0.009	501636.3	14658.3
6000	0.006	518259.9	14037.6

in Equations 25 and 26 in Chapter 3 can be determined, resulting in Equations 47 and 48, which are used to predict the thrust and torque in the secondary cutting zone.

$$K_{n,scz} = 207159.5\, t_c^{-0.55511}\, V^{-0.35926} \tag{47}$$

$$K_{t,scz} = 6419804.3\, t_c^{-0.33648}\, V^{-0.69707} \tag{48}$$

This formulation for the secondary cutting zone differs from previous work [2] in that the secondary cutting zone is directly calibrated instead of extrapolating the model calibrated for the cutting lips onto the secondary cutting zone.

4.2.2 Indentation Zone

Calibration of the indentation zone model is performed using pilot holes with radii equal to the calculated indentation zone radius for each test. Because the indentation zone radius calculation (see Equation 27) depends only on the feed, not on the speed, only three tests must be performed corresponding to the different feed values. The thrust and torque for these tests are used to solve for the yield shear stress (K) in Equation 28 in Chapter 3. For improved accuracy, the thrust forces are used instead of torque and the final yield shear stress is taken as the average value from the three tests. For the given experiments, the value of K is equal to 56,052.47 psi. In previous work [2], the thrust force due to the indentation zone was taken as the remaining

value after the thrust force due to the cutting lips and secondary cutting zone were subtracted from the total measured thrust force. In this work the indentation zone thrust force is experimentally determined as the thrust force due to the calculated indentation zone and then this thrust is used to calculate the yield shear stress of the workpiece material. The measured thrust force for the indentation zones and the corresponding yield shear stresses for each feed are listed in Table 9. The average yield shear stress value was used for the model.

Table 9: Yield Shear Stress Calculation

Indentation Zone Diameter (in)	**Feed (ipr)**	**Indentation Zone Thrust (lbf)**	**Yield Shear Stress (psi)**
0.0067	0.004	14.73	108052.22
0.0100	0.006	11.29	36981.45
0.0150	0.009	15.88	23123.74
		average K	56052.47

4.3 Validation

At the completion of the calibration tests, a number of tests are performed to evaluate the accuracy of the model using feed and speed combinations not used in the calibration tests. Calibration and validation tests are given in Tables 10 and 11 to evaluate the accuracy of the model. Within the calibration tests, the thrust error ranges from 2.67% up to 15.15% and the torque error ranges from -4.59% to -26.81%. In the validation tests, the thrust error ranges from -0.40% up to 7.96% while the torque error ranges from -15.55% to -22.87%. It is clear that the thrust model is accurate within the calibrated range, while the torque model is reasonably accurate, but consistently under predicts the measured torque. The discrepancy in measured and predicted torque forces could be due to the size of the drill. Because the total

torque values are small, if the model is off by 3 lbf-in this could be an 18% error. By using larger drills, the percentage error would be reduced by having an overall higher torque value. The model also assumes that there is no rubbing against the walls of the hole when the drill is fully engaged. This friction could cause an increase in torque beyond the expected values.

4.4 Step Drill Validation

Step drill geometry varies from the standard drill geometry by the addition of a secondary point angle and a step length between the point angle and the secondary point angle (see Figure 4 in Chapter 2). The inner diameter of the drill can also be modified so that a larger or smaller percentage of cutting can be performed by the secondary point angle in comparison to the primary point angle. In the mechanistic model modification for the step drill there is no change to the chisel edge model because the inner diameter of the drill is not decreased below the length of the chisel edge. The cutting lips section of the model is modified so that it is separated into two regions, the primary point angle and the secondary point angle, separated by the step length. These two point angles differ so the model must account for them. The step length has a constant diameter and is assumed to cause negligible thrust and torque. Table 12 displays the total predicted and measured thrust and torque produced by some step drill geometries. All of the drills have a primary point angle of 110 degrees and a diameter of 0.3156 in. In these validation tests, the average error in thrust prediction is 0.72% while the average error in torque prediction is -8.72%. This shows that the thrust model is accurate, while the torque model is accurate, but consistently under predicts the measured torque. This is consistent with the model's performance with the standard drill. The predicted and measured thrust and torque for a step drill are shown in Figures 23 and 24.

The step drill models shown do not include a pilot hole. Region 1 is the indentation

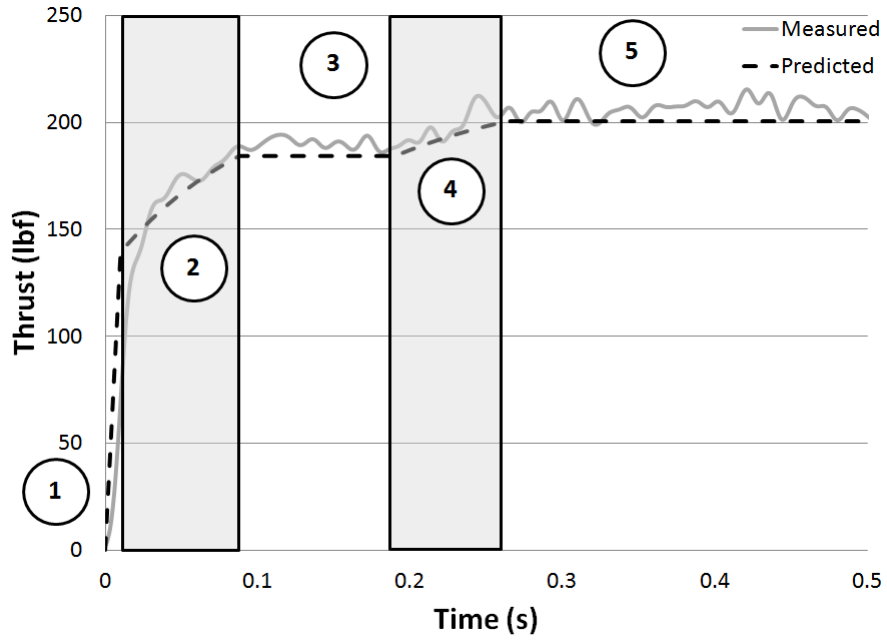

Figure 23: Predicted and Measured Thrust: Speed 4500 rpm, Feed 0.009 ipr, Inner Diameter 0.2 in, Step Angle 100 deg, Step Length 0.07 in

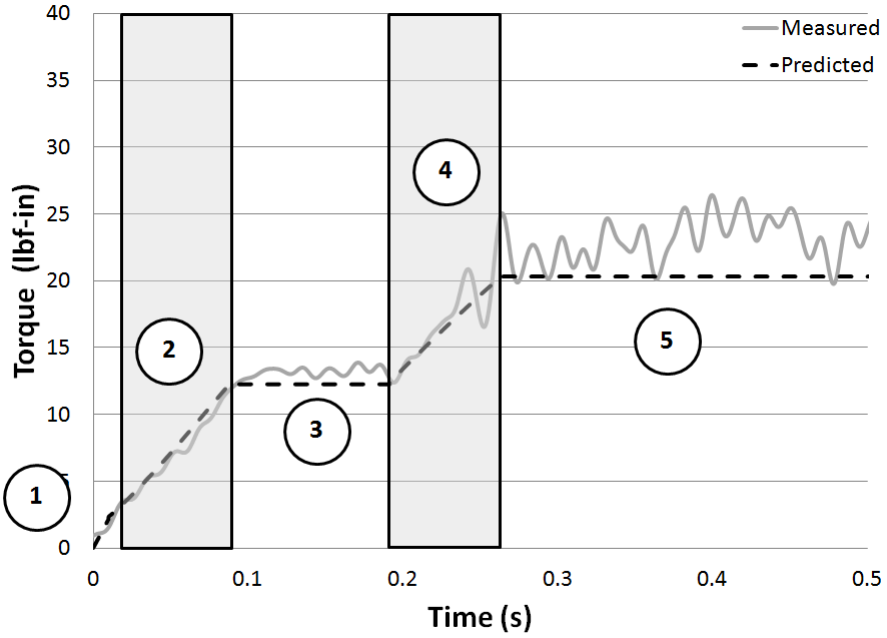

Figure 24: Predicted and Measured Torque: Speed 4500 rpm, Feed 0.009 ipr, Inner Diameter 0.2 in, Step Angle 100 deg, Step Length 0.07 in

zone and secondary cutting zone on the chisel edge. The primary point angle engages in section 2. In section 3 the primary point angle is fully engaged and the step length is engaging. In the fourth region the step angle is entering the workpiece. The drill is fully engaged in section 5.

4.4.1 Effects of Step Drill Geometry on Thrust and Torque

The effect of secondary point angle and inner diameter are investigated using the validated step drill model. The relationship between secondary point angle and predicted thrust and torque is shown in Figures 25 and 26. The total thrust and torque were predicted using two different inner diameter values, 0.1 in and 0.2 in, in order to display the changing relationship between secondary point angle and thrust and torque. As shown, the slope changes between the inner diameter values. For either inner diameter value, the thrust increases as the secondary point angle is increased, and the torque decreases.

In Figures 27 and 28 the relationship between inner diameter and thrust and torque is shown. The relationship is shown for two different step angles, 70 and 90 degrees, both of which are smaller than the primary point angle of 110 degrees. As the inner diameter is increased, the thrust increases for both step angles while the torque decreases for both.

4.5 Summary

In this section the experimental procedure was explained for calibrating and validating the mechanistic model. A number of tests were completed for a variety of speed and feed combinations with pilot holes ranging in size from the diameter of the indentation zone up to the length of the chisel edge so that the thrust and torque due to different regions on the drill could be isolated. The model was also modified to accept the geometry associated with a step drill so that thrust and torque caused by a step drill could be predicted. Burrs caused by drilling will be discussed in the following

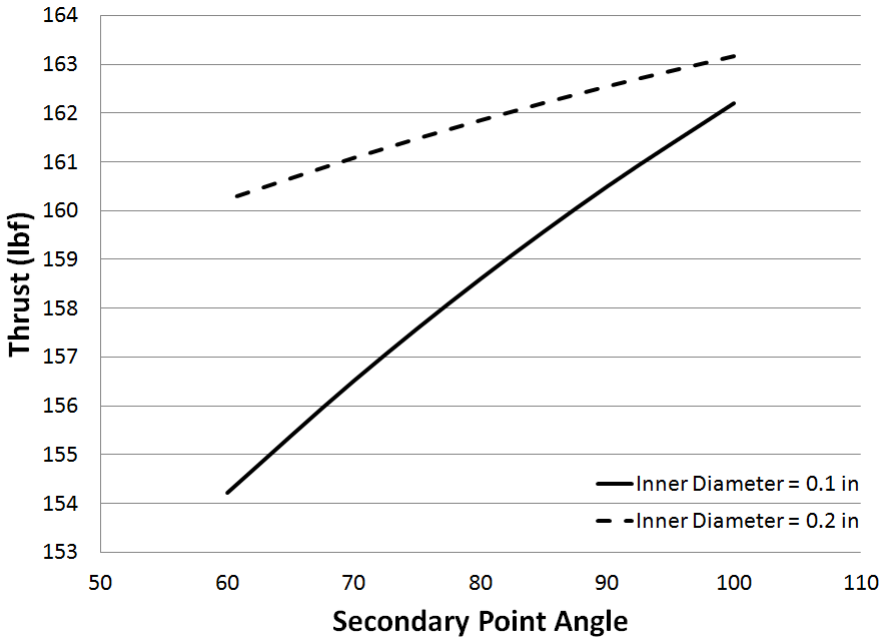

Figure 25: Predicted Thrust with Varying Secondary Point Angle: Speed 4500 rpm, Feed 0.006 ipr, Step Length 0.07 in

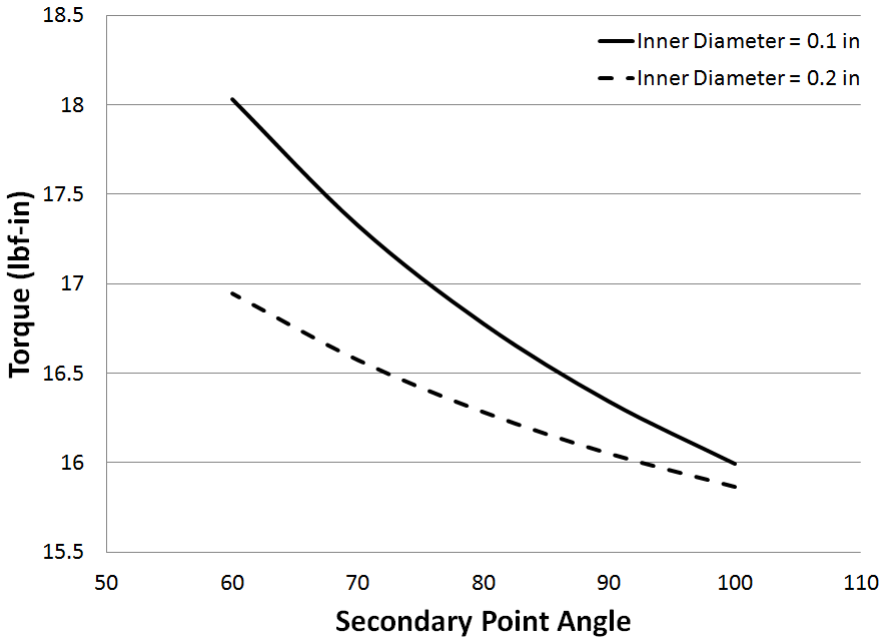

Figure 26: Predicted Torque with Varying Secondary Point Angle: Speed 4500 rpm, Feed 0.006 ipr, Step Length 0.07 in

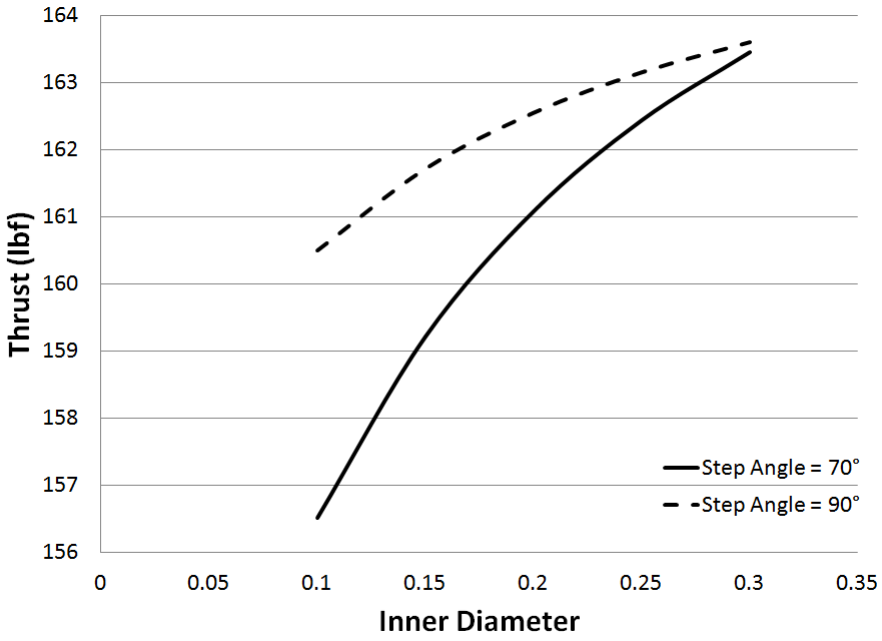

Figure 27: Predicted Thrust with Varying Inner Diameter: Speed 4500 rpm, Feed 0.006 ipr, Step Length 0.07 in

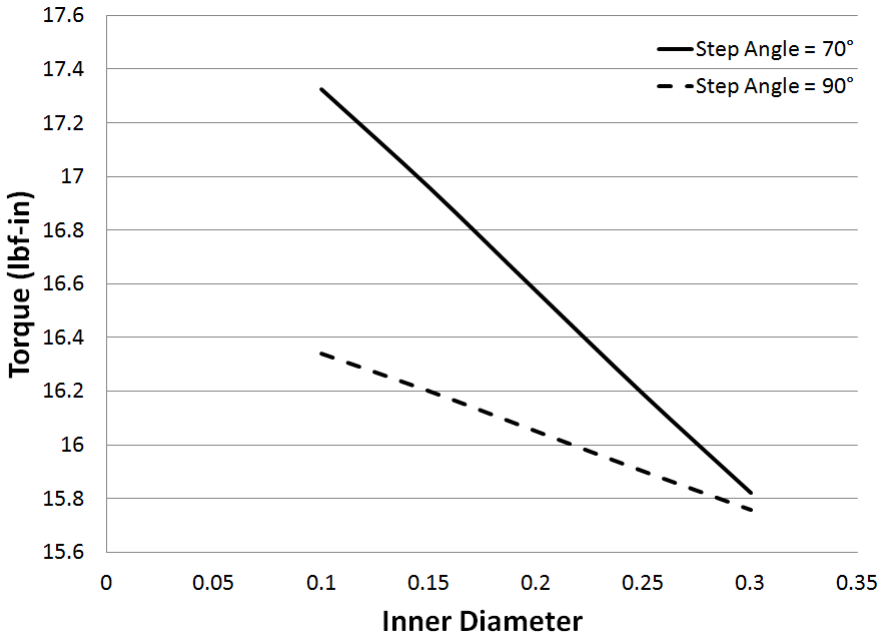

Figure 28: Predicted Torque with Varying Inner Diameter: Speed 4500 rpm, Feed 0.006 ipr, Step Length 0.07 in

chapter, including the implementation of this mechanistic model into an evaluation of potential modifications to the step drill geometry and experimental conditions to reduce burr heights.

Table 10: Experimental and Predicted Thrust and Torque - Calibration Tests

		Indentation Zone		**Secondary Cutting Zone**		**Chisel Edge Total**		**Cutting Lips**		**Total**	
Speed (rpm)	**Feed (ipr)**	**Thrust (lbf)**	**Torque (lbf-in)**	**Thrust (lbf)**	**Torque (lbf-in)**	**Thrust (lbf)**	**Torque (lbf-in)**	**Thrust (lbf)**	**Torque (lbf-in)**	**Thrust (lbf)**	**Torque (lbf-in)**
3000	0.006	14.66	0.029	114.85	2.22	129.51	2.25	46.03	13.73	175.55	15.98
Experimental						*108.24*	*6.01*	*44.22*	*15.82*	*152.46*	*21.83*
4500	0.004	6.52	0.009	90.73	1.32	97.24	1.33	39.17	10.95	136.41	12.28
Experimental						*90.07*	*2.79*	*35.92*	*10.08*	*125.99*	*12.87*
4500	0.006	14.66	0.029	99.28	1.67	113.94	1.70	49.76	14.01	163.71	15.71
Experimental						*105.24*	*2.15*	*49.47*	*17.61*	*154.71*	*19.76*
4500	0.009	32.99	0.097	104.81	2.08	137.80	2.17	63.22	17.93	201.02	20.10
Experimental						*136.19*	*2.94*	*59.61*	*23.17*	*195.80*	*26.10*
6000	0.006	14.66	0.029	89.53	1.37	104.20	1.40	52.59	14.22	156.79	15.61
Experimental						*100.15*	*1.47*	*51.27*	*16.98*	*151.43*	*18.45*

Table 11: Experimental and Predicted Thrust and Torque - Validation Tests

		Indentation Zone		**Secondary Cutting Zone**		**Chisel Edge Total**		**Cutting Lips**		**Total**	
Speed (rpm)	**Feed (ipr)**	**Thrust (lbf)**	**Torque (lbf-in)**	**Thrust (lbf)**	**Torque (lbf-in)**	**Thrust (lbf)**	**Torque (lbf-in)**	**Thrust (lbf)**	**Torque (lbf-in)**	**Thrust (lbf)**	**Torque (lbf-in)**
3500	0.005	10.18	0.017	104.71	1.80	114.89	1.81	42.58	12.38	157.47	14.20
Experimental						*104.75*	*3.92*	*41.11*	*13.40*	*145.86*	*17.32*
4000	0.008	26.06	0.068	108.16	2.12	134.22	2.19	57.66	16.59	191.88	18.78
Experimental						*131.72*	*4.30*	*57.84*	*20.05*	*189.57*	*24.35*
5000	0.007	19.96	0.046	98.10	1.69	118.05	1.74	55.62	15.47	173.67	17.21
Experimental						*119.93*	*1.41*	*53.07*	*19.43*	*173.01*	*20.84*
5500	0.005	10.18	0.017	89.02	1.31	99.20	1.33	46.44	12.67	145.64	14.00
Experimental						*100.90*	*1.08*	*45.33*	*15.49*	*146.22*	*16.57*

Table 12: Step Drill Validation Tests - Primary Point Angle 110 deg, Drill Diameter 0.3156 in

Secondary Point Angle (deg)	**Inner Diameter (in)**	**Speed (rpm)**	**Feed (ipr)**	**Thrust (lbf)**	**Torque (lbf-in)**
60	0.1	3000	0.009	201.56	23.32
Experimental				*200.36*	*25.10*
60	0.1	5500	0.005	136.78	16.09
Experimental				*152.82*	*17.58*
80	0.1	4000	0.008	185.96	20.04
Experimental				*222.34*	*21.35*
80	0.1	5000	0.007	167.96	18.38
Experimental				*207.30*	*19.14*
60	0.2	3500	0.005	154.49	15.28
Experimental				*127.51*	*15.54*
60	0.2	6000	0.006	153.11	16.86
Experimental				*136.58*	*18.54*
80	0.2	4000	0.008	189.73	19.45
Experimental				*178.53*	*22.17*
80	0.2	5500	0.005	143.91	14.51
Experimental				*144.06*	*16.16*
100	0.2	3500	0.005	157.01	14.33
Experimental				*144.22*	*15.19*
100	0.2	4500	0.009	200.34	20.29
Experimental				*202.73*	*24.12*

CHAPTER V

BURR MEASUREMENT AND ANALYSIS

This chapter begins by discussing the burr measurement procedure and then continues to the analysis. Burr height, thrust and torque are examined for holes drilled while varying the following parameters.

- Secondary point angle ($2sk$)
- Inner diameter (iD)
- Feed (f)
- Speed (N)

Earlier research is also addressed in this section highlighting similarities, differences and new information. The step drills referenced in the following sections have a primary point angle of 110 degrees and an outer diameter of 0.3156 in.

5.1 Burr Measurement

Experimental tests are performed to collect force data for validation or analysis purposes and to measure hole exit burr heights. Burrs are measured using a 3D laser confocal microscope (LEXT OLS4000, Olympus Corp.). Foam is inserted within the drilled hole to reduce the measurement noise in the region. Profile data for each test is recorded and burr heights are measured at 36 points along the circumference of the hole as shown in Figure 29. A line is created perpendicular to the edge of the hole, the workpiece surface is chosen as a reference and the cursor is aligned with the peak of the burr. The burr height is measured as the vertical difference between these two values. Figure 30 shows the typical variation in burr height along the circumference

of the hole. In all further discussions the average burr height for all points of an experiment is considered.

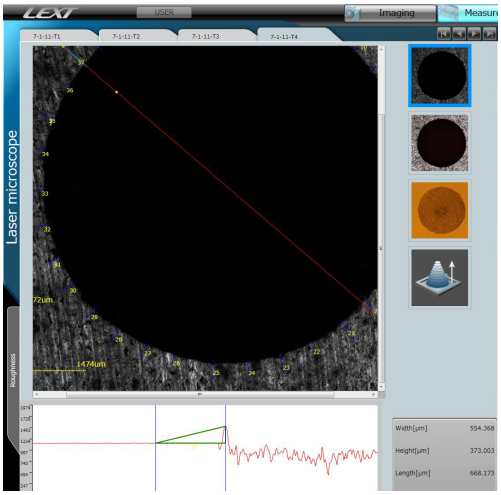

Figure 29: Burr Measurement Using Confocal Microscope

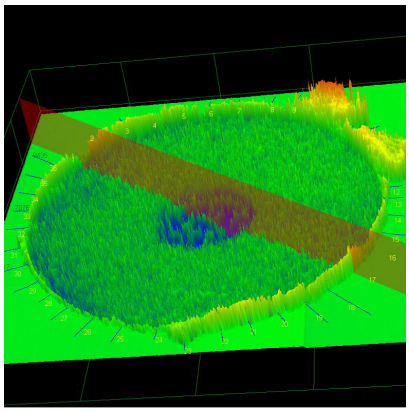

Figure 30: Surface View of Burr Distribution

5.2 Effect of Secondary Point Angle

In this section burr data is compared for tests that have the same feed, speed and inner diameter, but have different secondary point angles. Table 13 gives the experimental data for three tests performed at 3500 rpm and 0.005 ipr with an inner diameter

measurement of 0.2 in. It also shows the comparison with the standard twist drill without a step. It is clearly shown that adding the step significantly decreases the burr height.

Table 13: Secondary Point Angle Tests

Speed (rpm)	**Feed (ipr)**	**Secondary Point Angle (degrees)**	**Inner Diameter (in)**	**Thrust (lbf)**	**Torque (lbf-in)**	**Average Burr Height (in)**
3500	0.005	60	0.2	127.51	15.54	0.0048
3500	0.005	80	0.2	145.23	17.13	0.0043
3500	0.005	100	0.2	148.92	16.01	0.0011
3500	0.005	N/A	N/A	158.40	16.68	0.0157

The thrust, torque and average burr height for the step drills and standard twist drill are shown in Figures 31 to 33. In these figures the error bars represent the standard deviation of the measured values in a single experiment. For the step drills with secondary point angles of 60, 80 and 100 degrees the thrust force increases and average burr height decreases as the secondary point angle increases, but the torque does not follow this trend. The standard twist drill has thrust and torque values greater than the step drills and creates a much larger burr.

While the thrust and average burr height display opposite trends, the thrust force shows a much larger increase from 60 to 80 degrees when compared to the increase from 80 to 100 degrees secondary point angle. The average burr height displays the inverse relation with a smaller decrease in burr height from 60 to 80 degrees and a much larger decrease in burr height from 80 to 100 degrees secondary point angle. This suggests that although the trends are the inverse of one another, as the secondary point angle is increased, the thrust force increase is not directly proportional to the decrease in the average burr height. This data is in line with previous research

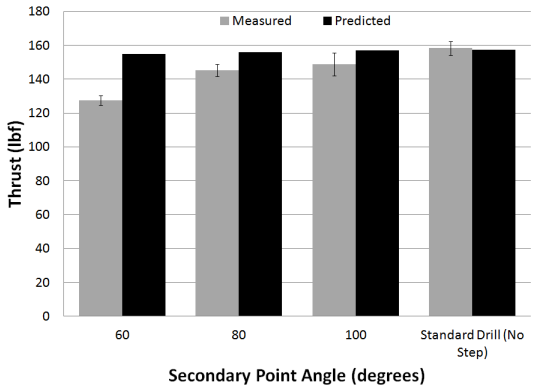

Figure 31: Effect of Secondary Point Angle on Thrust

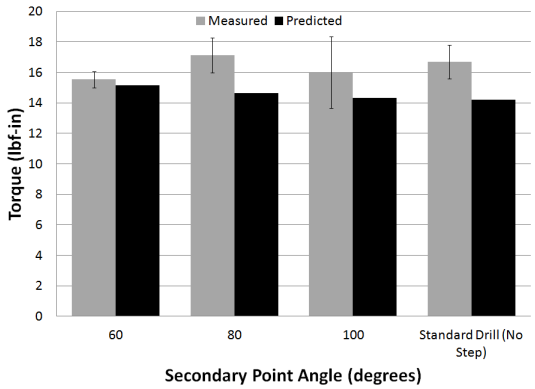

Figure 32: Effect of Secondary Point Angle on Torque

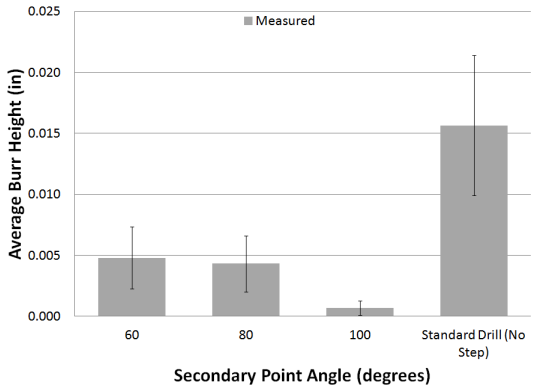

Figure 33: Effect of Secondary Point Angle on Average Burr Height

that concludes that a larger point angle minimizes burr height [16]. In this set of experiments the torque reaches its greatest value at the secondary point angle of 80 degrees, giving a trend shown in Figure 32 that is not similar to either trend for the thrust or average burr height. Because of the clear reduction in burr height by adding the step, the following studies focus exclusively on step drills.

5.3 Effect of Inner Diameter Size

Results for variation in thrust force, torque and average burr height with change in inner diameter are shown in Table 14. The trends for 60 degrees secondary point

Table 14: Inner Diameter Tests

Speed (rpm)	**Feed (ipr)**	**Secondary Point Angle (degrees)**	**Inner Diameter (in)**	**Thrust (lbf)**	**Torque (lbf-in)**	**Average Burr Height (in)**
3500	0.005	60	0.1	146.18	19.19	0.0032
3500	0.005	60	0.2	127.51	15.53	0.0048
4000	0.008	80	0.1	222.34	21.35	0.0038
4000	0.008	80	0.2	178.53	22.17	0.0027

angle are shown in Figures 34 to 36 and the trends for 80 degrees secondary point angle are displayed in Figures 37 to 39. In all figures the error bars represent the standard deviation of the thrust, torque or burr height within a single test.

For both secondary point angles the thrust force decreases as the inner diameter is increased. This does not align with what the force model predicts. Because the secondary point angles are both less than the primary point angle, if the inner diameter is increased, the thrust should also increase. One cause for this discrepancy could be drill wear, because the test for 60 degrees secondary point angle and 0.1 in inner diameter was one of the last tests performed using that drill. The drill wear

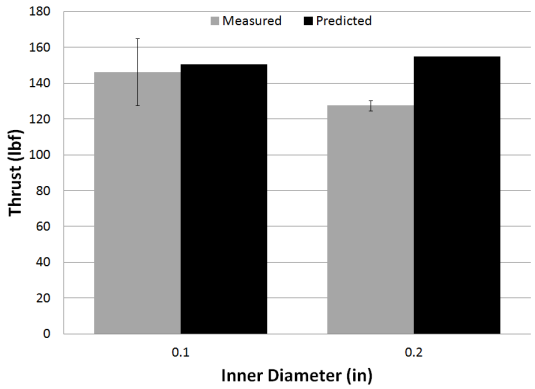

Figure 34: Effect of Inner Diameter on Thrust - 60 degrees Secondary Point Angle

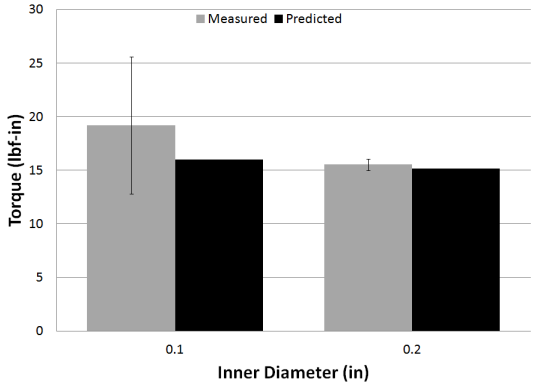

Figure 35: Effect of Inner Diameter on Torque - 60 degrees Secondary Point Angle

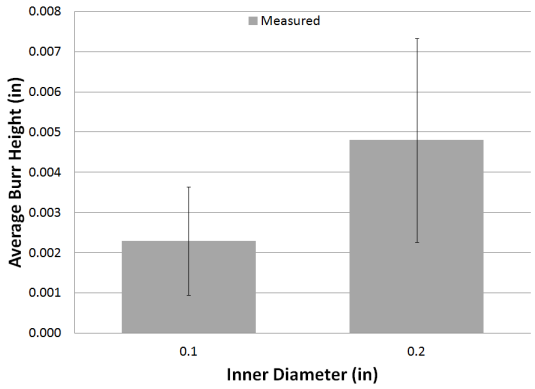

Figure 36: Effect of Inner Diameter on Average Burr Height - 60 degrees Secondary Point Angle

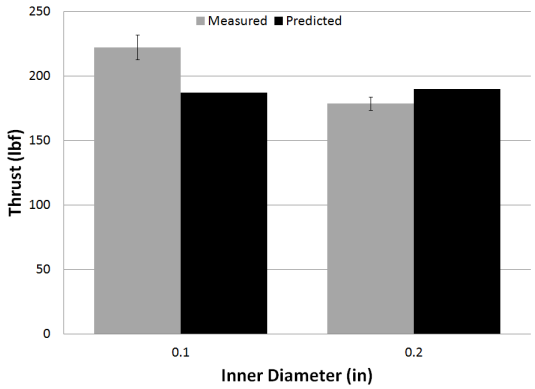

Figure 37: Effect of Inner Diameter on Thrust - 80 degrees Secondary Point Angle

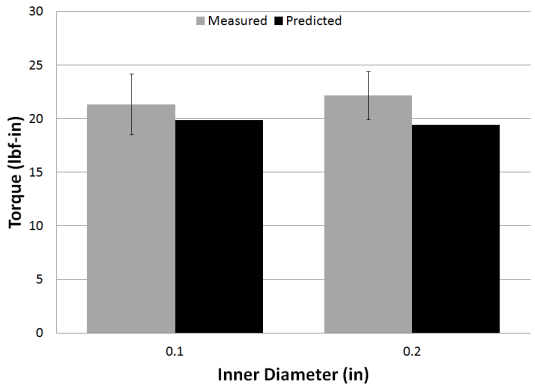

Figure 38: Effect of Inner Diameter on Torque - 80 degrees Secondary Point Angle

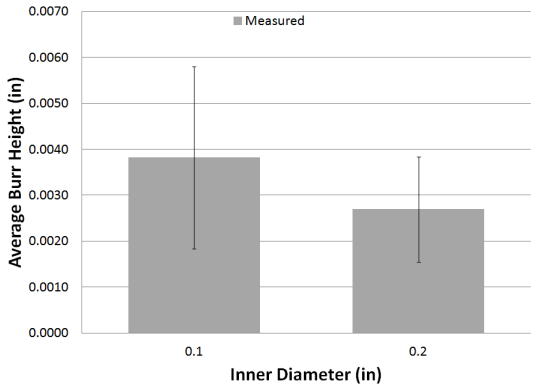

Figure 39: Effect of Inner Diameter on Average Burr Height - 80 degrees Secondary Point Angle

was not monitored or measured during experimental testing. Another cause for the discrepancy is the combination of 80 degrees secondary point angle and 0.1 in inner diameter resulted in poor chip evacuation while drilling. In multiple tests with this drill, the chips loaded the drill during the experiments, becoming stuck in the flutes and causing the drill temperature to sharply increase potentially causing the drill to wear prematurely leading to higher thrust forces.

Although the torque for the different point angle tests appears to showcase opposite trends, the difference in torque is 1-4 lbf-in between the different inner diameter values, which is not significant when the error of the measures is considered. The relationship between burr height and inner diameter is unclear due to high variation in the results. Also, according to Ko et al. [15] the difference between the inner and outer diameter does not have a significant impact on the burr height, which is in agreement with the current results.

5.4 Effect of Speed

Prior works have postulated that speed is insignificant in burr minimization [14] but the results of experiments in this work suggest that this is not completely true. In the tests performed with the 60 degree secondary point angle drills, the burr height increases with an increase in speed (see Figure 42). Due to the high errors in the tests with the 80 degree secondary point angle it is unclear if it follows the same trend as the 60 degree secondary point angle test. The thrust values for these tests display opposite trends, suggesting that changes in thrust with changing speeds may not correlate directly with burr heights.

The pair of tests with a 60 degree secondary point angle show an increase in thrust and burr height with an increase in speed as shown in Figures 40 to 42. When the secondary point angle was increased from 60 to 80 degrees the trend between average burr height and speed becomes unclear. This is displayed in Figures 43 to 45 and the

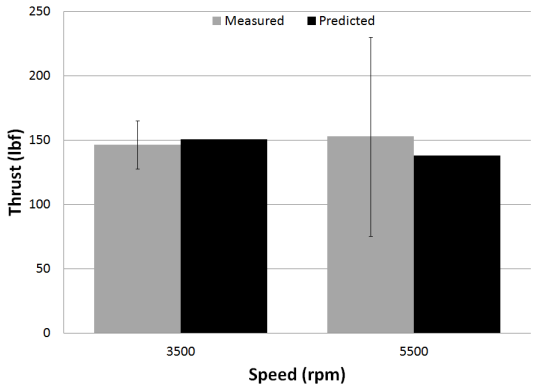

Figure 40: Effect of Speed on Thrust - 60 degrees Secondary Point Angle

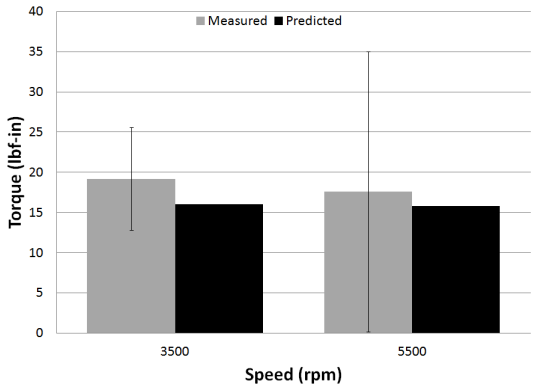

Figure 41: Effect of Speed on Torque - 60 degrees Secondary Point Angle

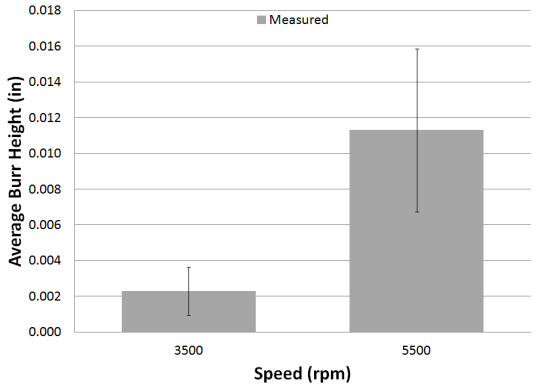

Figure 42: Effect of Speed on Average Burr Height - 60 degrees Secondary Point Angle

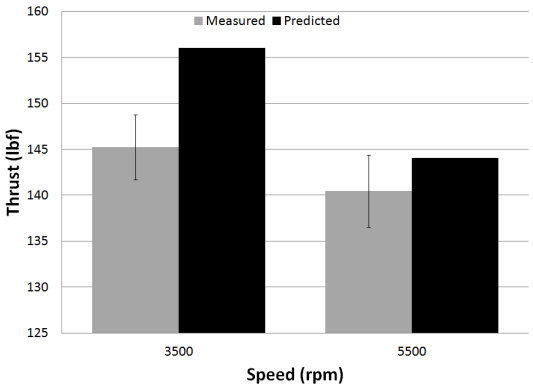

Figure 43: Effect of Speed on Thrust - 80 degrees Secondary Point Angle

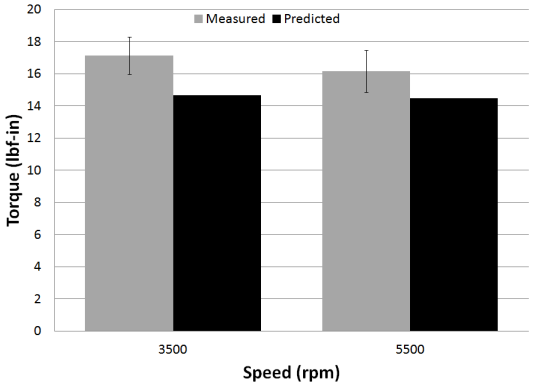

Figure 44: Effect of Speed on Torque - 80 degrees Secondary Point Angle

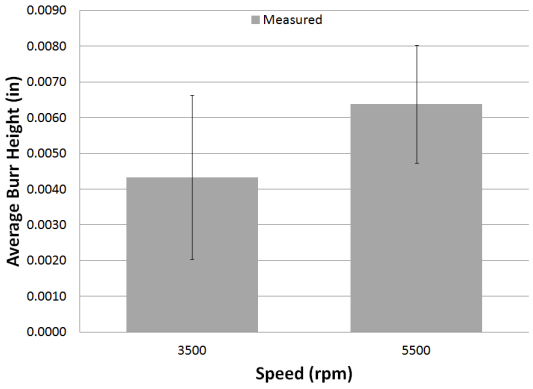

Figure 45: Effect of Speed on Average Burr Height - 80 degrees Secondary Point Angle

experimental data for these tests is given in Table 15.

Table 15: Speed Tests

Speed (rpm)	Feed (ipr)	Secondary Point Angle (degrees)	Inner Diameter (in)	Thrust (lbf)	Torque (lbf-in)	Average Burr Height (in)
3500	0.005	60	0.1	146.18	19.19	0.0032
5500	0.005	60	0.2	152.82	17.58	0.0113
3500	0.005	80	0.2	145.23	17.13	0.0043
5500	0.005	80	0.2	140.45	16.15	0.0064

Results for variation in burr height with speed agree with results from a previous study by Kilickap and Huseyinoglu [12]. In another work by Ko et al. [14] the authors assume that the speed does not affect burr height. The results for variation in torque when the increasing in speed show a decreasing trend which is the opposite of the trend in burr height.

5.5 Effect of Feed

Tests were performed at various feeds using two different speed and secondary point angle pairs. For the tests performed at 100 degrees secondary point angle, the burr height appears to decrease and then remain constant or increase as the feed is increased. There are only two tests for 80 degrees secondary point angle and the burr height either decreases or remains constant as the feed increases. Because there are only two tests, the trend is uncertain. In the paper by Pande and Relekar [21] the burr height initially decreased and then increased leading the authors to propose that there is an optimum feed range which minimizes burr height. Kilickap and Huseyinoglu [12] observed that an increase in feedrate caused an increase in burr height as a result of an increase in thrust force. For both secondary point angles the thrust force and

torque increase with an increase in feed. A table of the experimental testing data is given in Table 16. The thrust, torque and average burr height for these tests are given in Figures 46 to 51. In the figures, the standard deviation of a single experiment is represented by the error bars on the measurement.

Table 16: Feed Tests

Speed (rpm)	**Feed (ipr)**	**Secondary Point Angle (degrees)**	**Inner Diameter (in)**	**Thrust (lbf)**	**Torque (lbf-in)**	**Average Burr Height (in)**
4000	0.004	80	0.2	130.52	14.91	0.0047
4000	0.008	80	0.2	178.53	22.17	0.0027
4500	0.003	100	0.2	116.07	11.99	0.0122
4500	0.006	100	0.2	169.52	18.80	0.0032
4500	0.009	100	0.2	202.73	24.12	0.0037

5.6 Summary

This chapter presented the results of an experimental study of the effect of speed, feed, step drill inner diameter and secondary point angle on burr height, thrust force and torque. It is concluded that with an increase in secondary point angle and resulting increase in thrust force, there is a decrease in average burr height. The trend between the inner diameter and burr height is unclear, while the thrust forces in that test show a trend that is different than that predicted by the model. The experimental results show a decrease in thrust force as the inner diameter is increased, while the model predicts an increase in thrust force. As the speed increases, the burr height increases for the smaller secondary point angle. However, for the larger secondary point angle, the trend is uncertain. The relationship between the other parameters is unclear. The following chapter will discuss the conclusions and recommendations resulting from this research.

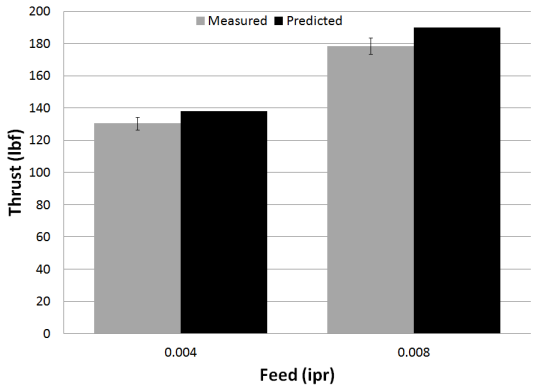

Figure 46: Effect of Feed on Thrust - 80 degrees Secondary Point Angle, 4000 rpm

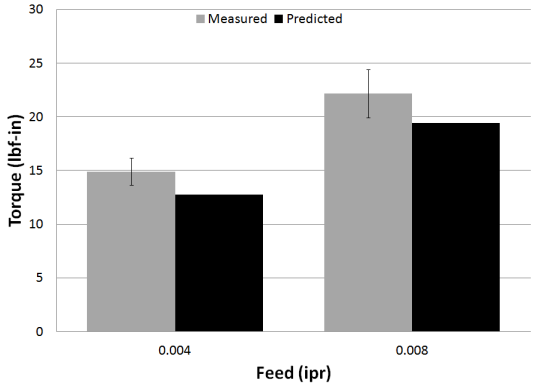

Figure 47: Effect of Feed on Torque - 80 degrees Secondary Point Angle, 4000 rpm

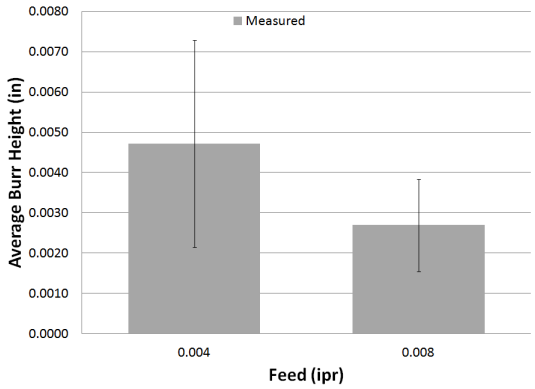

Figure 48: Effect of Feed on Average Burr Height - 80 degrees Secondary Point Angle, 4000 rpm

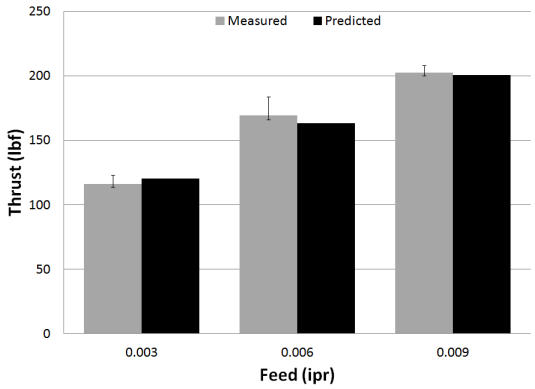

Figure 49: Effect of Feed on Thrust - 100 degrees Secondary Point Angle, 4500 rpm

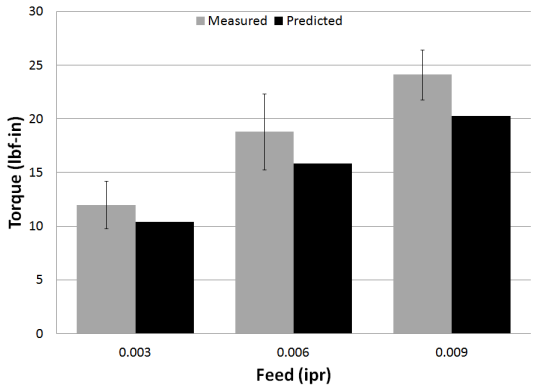

Figure 50: Effect of Feed on Torque - 100 degrees Secondary Point Angle, 4500 rpm

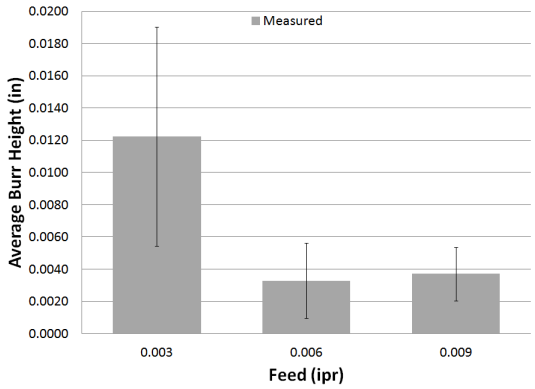

Figure 51: Effect of Feed on Average Burr Height - 100 degrees Secondary Point Angle, 4500 rpm

CHAPTER VI

CONCLUSIONS AND RECOMMENDATIONS

The primary objective of this thesis was to develop, calibrate and validate a mechanistic force model for drilling that was then adapted to predict the thrust and torque produced when drilling with a step drill. Currently, empirical models have been the only type of model developed for step drills, so a mechanistic model was developed in this thesis as an improvement over past models. The resulting model was used in conjunction with experiments to investigate the relationship between secondary point angle, inner diameter, speed and feed and average burr height. It is shown that by using a step drill the burr height is greatly reduced when compared to a standard twist drill and there is a decrease in the thrust force as well.

The mechanistic model for drilling with a step drill was validated to predict the thrust and torque within reasonable errors. This model was developed by modifying and improving on a mechanistic model developed by Chandrasekharan [2]. Improvements were made to the calibration process for the chisel edge of the drill to better predict the thrust and torque produced by the secondary cutting zone and indentation zone. Within the calibration tests, the thrust error ranges from 2.67% up to 15.15% and the torque error ranges from -4.59% to -26.81%. In the validation tests, the thrust error ranges from -0.40% up to 7.96% while the torque error ranges from -15.55% to -22.87%. It is clear that the thrust model is accurate within the calibrated range, while the torque model is reasonably accurate, but consistently under predicts the measured torque. The model was adapted to predict the thrust and torque produced by a step drill. This included the separation of the cutting lips into two sections with two different point angles, separated by the step length. In these validation tests, the

average error in thrust prediction is 0.72% while the average error in torque prediction is -8.72%. This shows that the thrust model is accurate, and the torque model is accurate, but consistently under predicts the measured torque.

Experiments were performed to study the relationship between burrs produced when drilling with step drills of different secondary point angle, inner diameter, speed and feed values. It is concluded that using a step drill instead of a standard drill leads to a reduction in thrust force and burr height. However, further modification of the step drill geometry to reduce thrust force does not always result in a decrease in burr height.

Furthermore, it is concluded that as the secondary point angle is increased, the thrust is increased and the burr height is decreased. When tests were performed varying feed, as the feed increased, there was a direct increase in thrust, but the trend in burr height was uncertain. These conclusions shed light on the complex interaction between drill geometry, drilling process parameters, drilling forces and burr height. Although previous researchers theorize that reduction in burr height can be achieved by reducing thrust force, the results suggest that future studies involving varying drill geometries and process parameters are necessary to examine the relationship between burr height and thrust force.

To further increase knowledge regarding the relationship between burr height and step drill geometry, speed and feed the following are suggested for future work.

- Investigation of the relationship between step angles and tool wear with varying inner diameters
- Analysis of chip flow by varying secondary point angle, inner diameter and helix angle to understand if some drill geometries are less efficient for chip evacuation
- Investigation between step drill geometry and speed and feed to determine if some combinations result in significant oscillations and how to predict them

- Study of the effect on burr height when adding a split point to the step drills
- Investigation of the resulting burr height using step drills of different materials such as carbides, or adding coatings

APPENDIX A

TWIST DRILL CALIBRATION TESTS

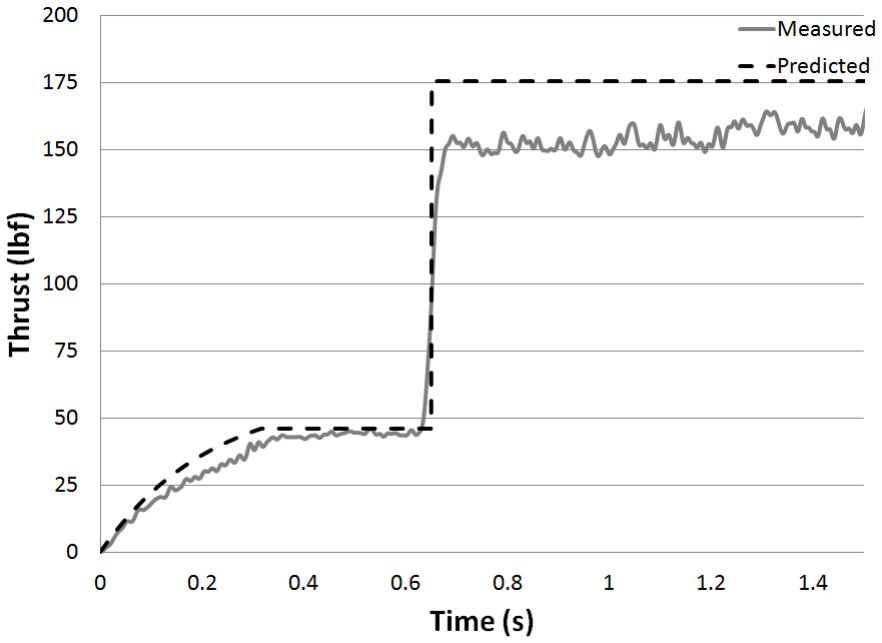

Figure 52: Predicted and Measured Thrust: Speed 3000 rpm, Feed 0.006 ipr

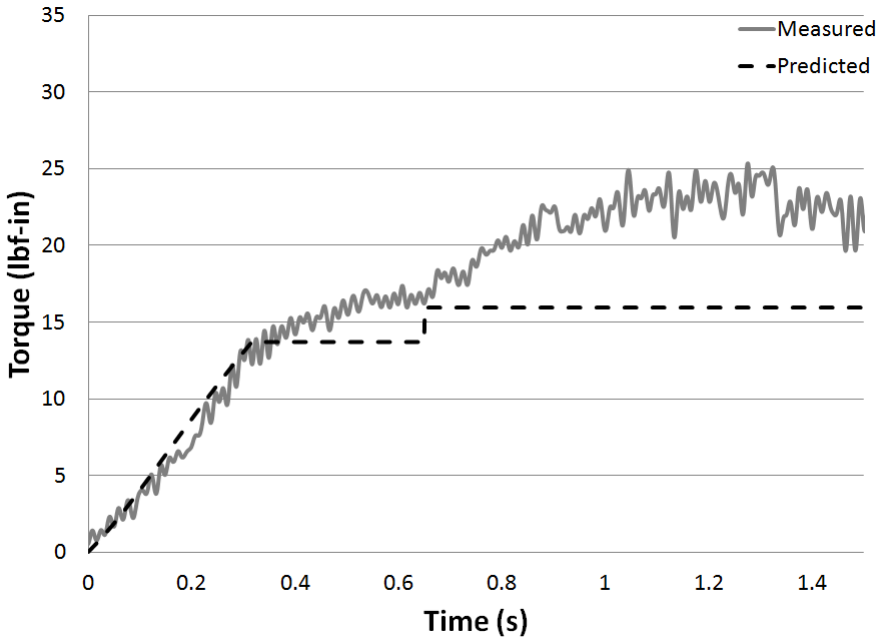

Figure 53: Predicted and Measured Torque: Speed 3000 rpm, Feed 0.006 ipr

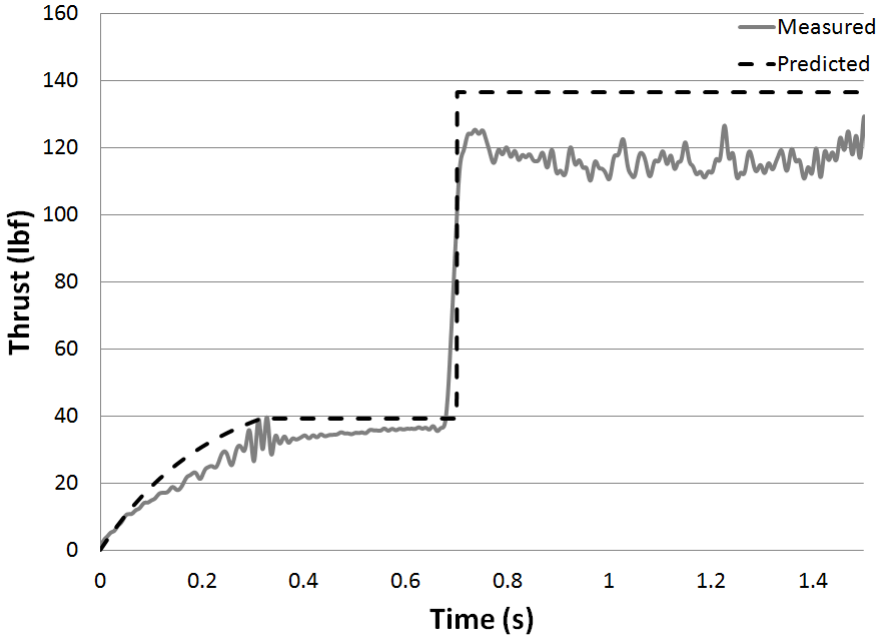

Figure 54: Predicted and Measured Thrust: Speed 4500 rpm, Feed 0.004 ipr

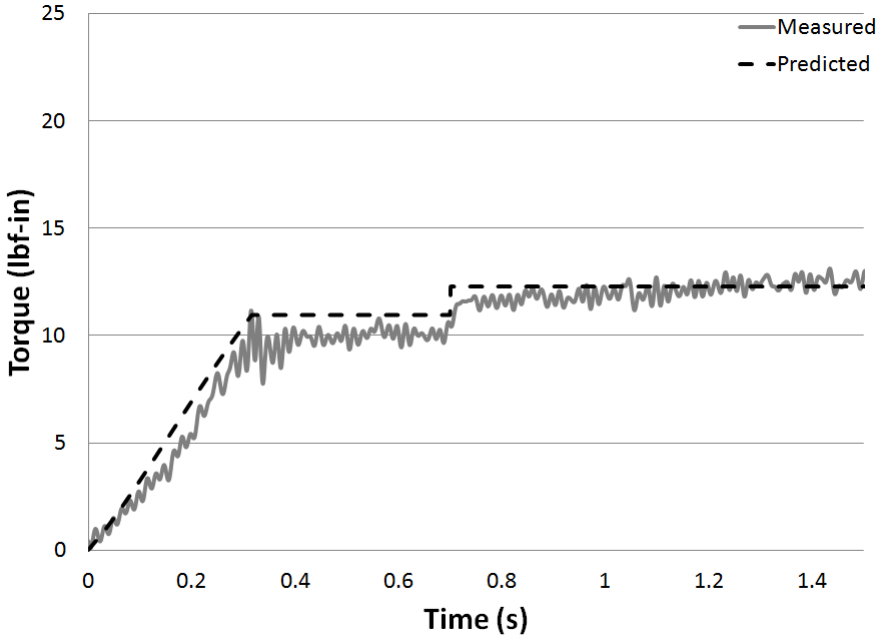

Figure 55: Predicted and Measured Torque: Speed 4500 rpm, Feed 0.004 ipr

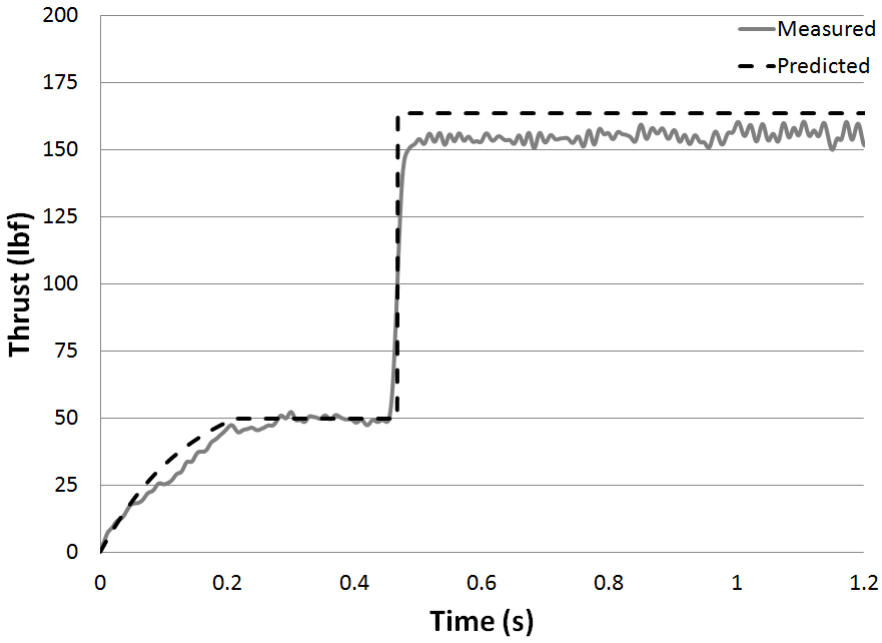

Figure 56: Predicted and Measured Thrust: Speed 4500 rpm, Feed 0.006 ipr

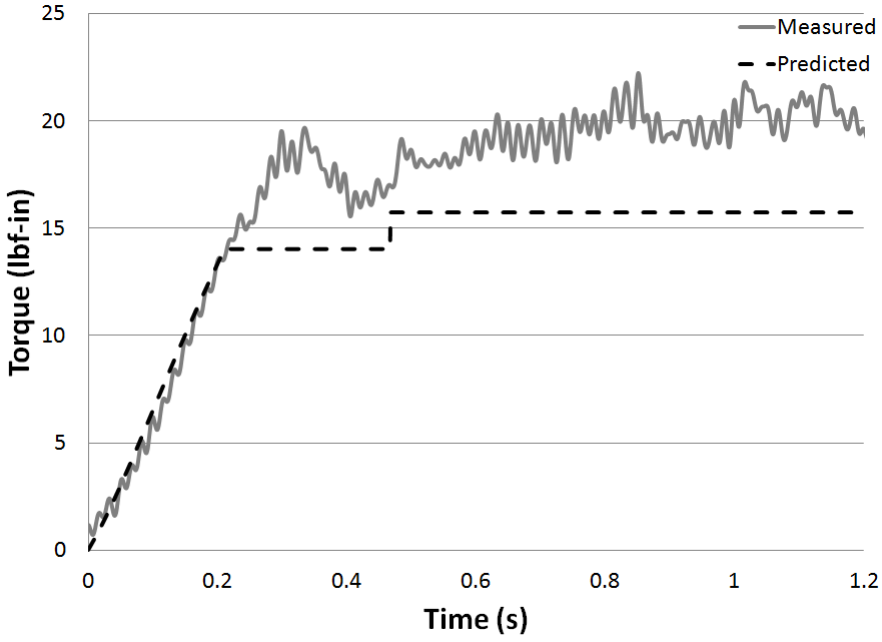

Figure 57: Predicted and Measured Torque: Speed 4500 rpm, Feed 0.006 ipr

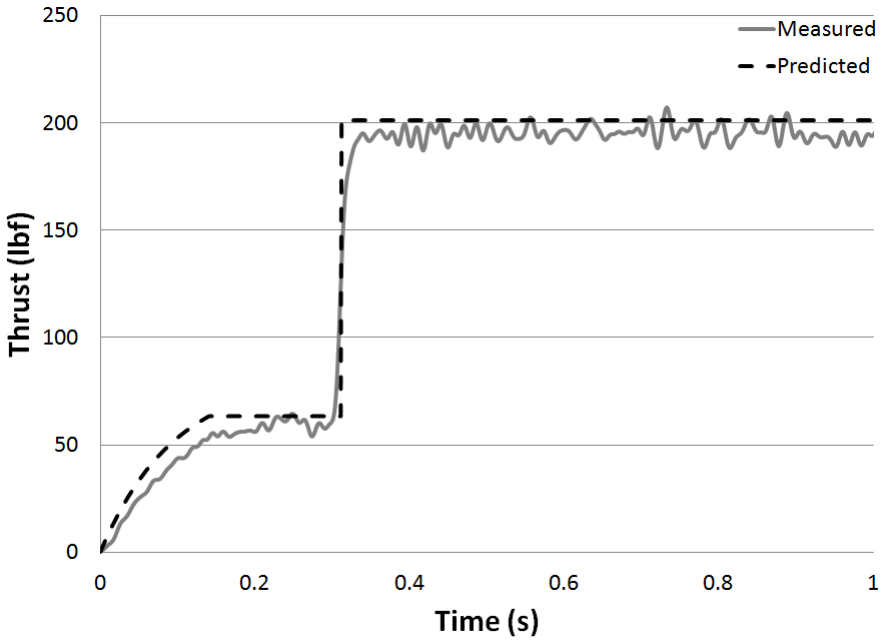

Figure 58: Predicted and Measured Thrust: Speed 4500 rpm, Feed 0.009 ipr

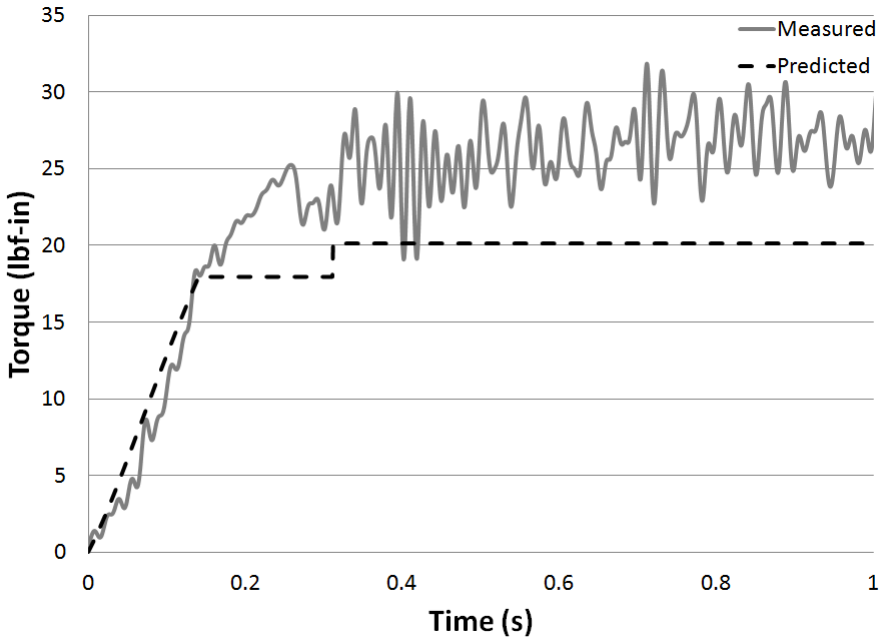

Figure 59: Predicted and Measured Torque: Speed 4500 rpm, Feed 0.009 ipr

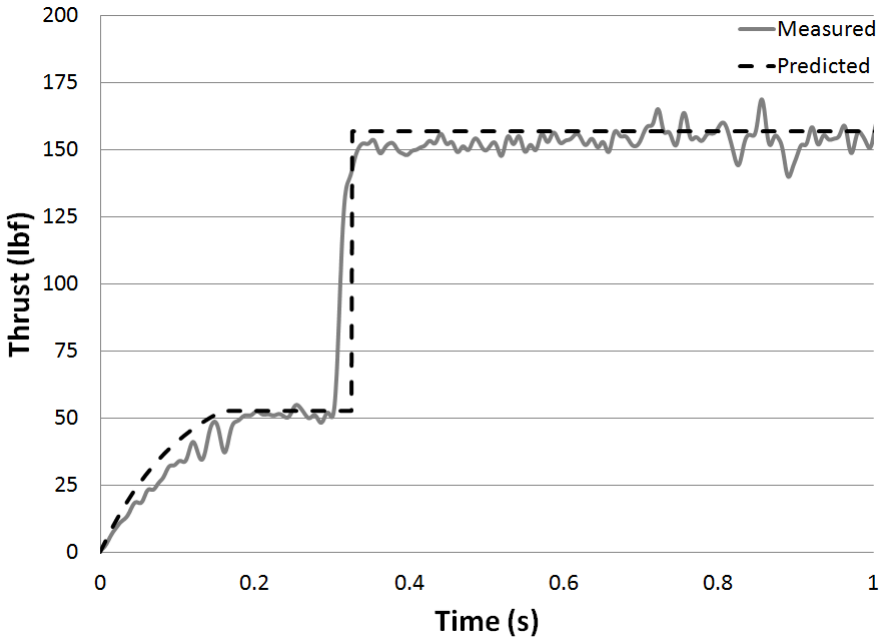

Figure 60: Predicted and Measured Thrust: Speed 6000 rpm, Feed 0.006 ipr

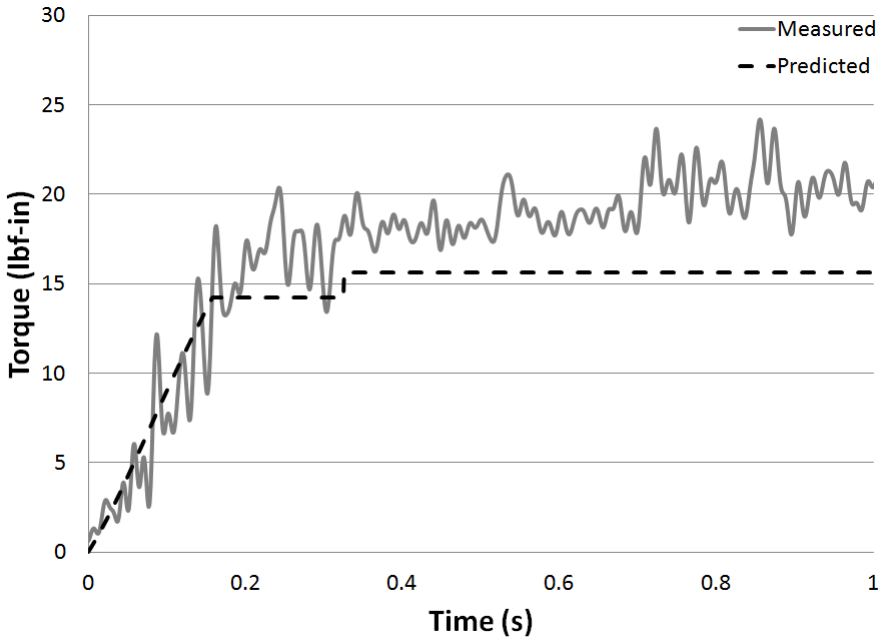

Figure 61: Predicted and Measured Torque: Speed 6000 rpm, Feed 0.006 ipr

APPENDIX B

TWIST DRILL VALIDATION TESTS

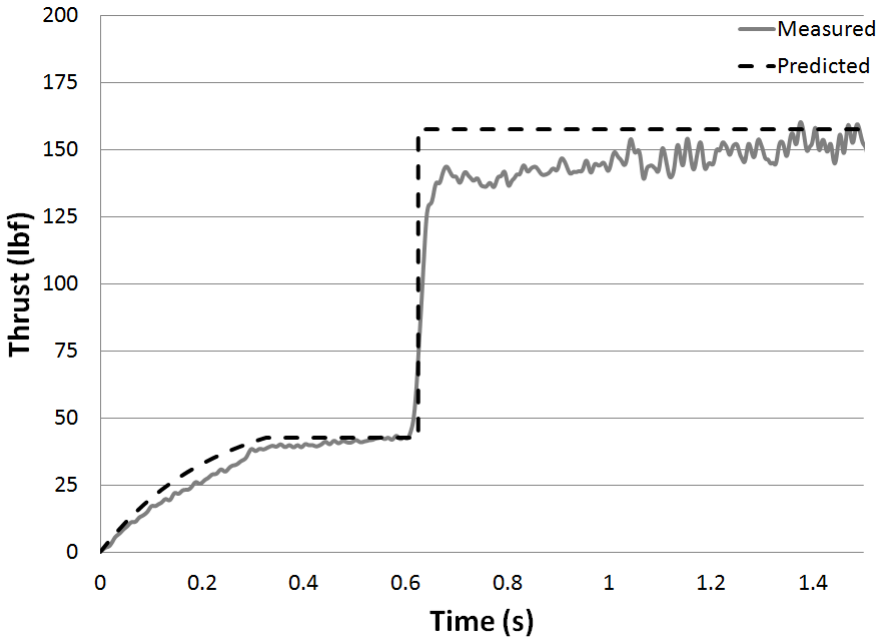

Figure 62: Predicted and Measured Thrust: Speed 3500 rpm, Feed 0.005 ipr

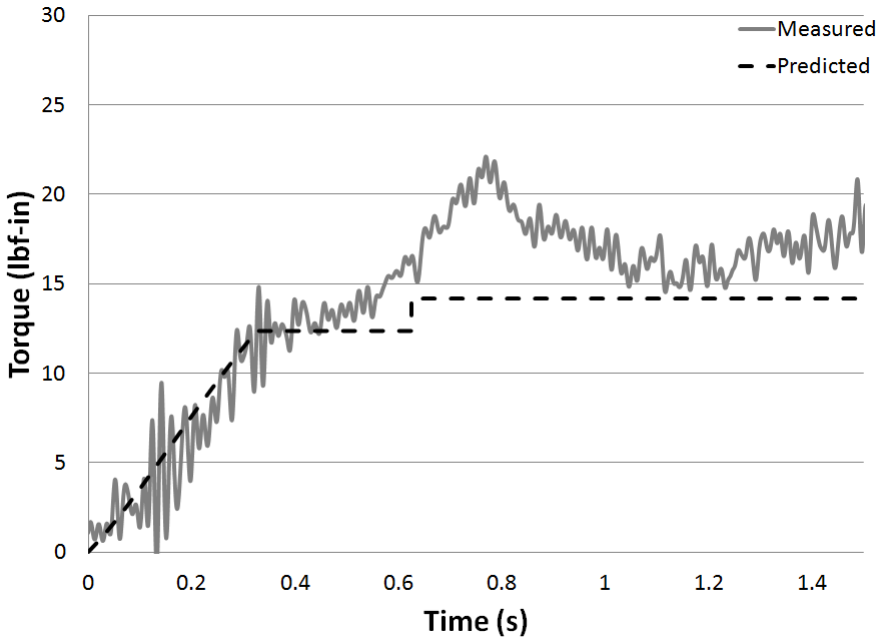

Figure 63: Predicted and Measured Torque: Speed 3500 rpm, Feed 0.005 ipr

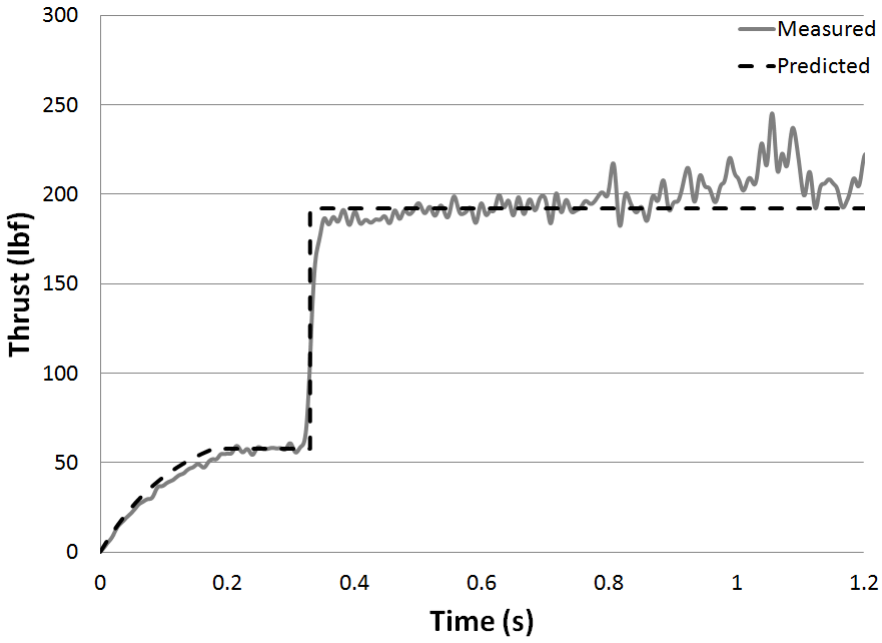

Figure 64: Predicted and Measured Thrust: Speed 4000 rpm, Feed 0.008 ipr

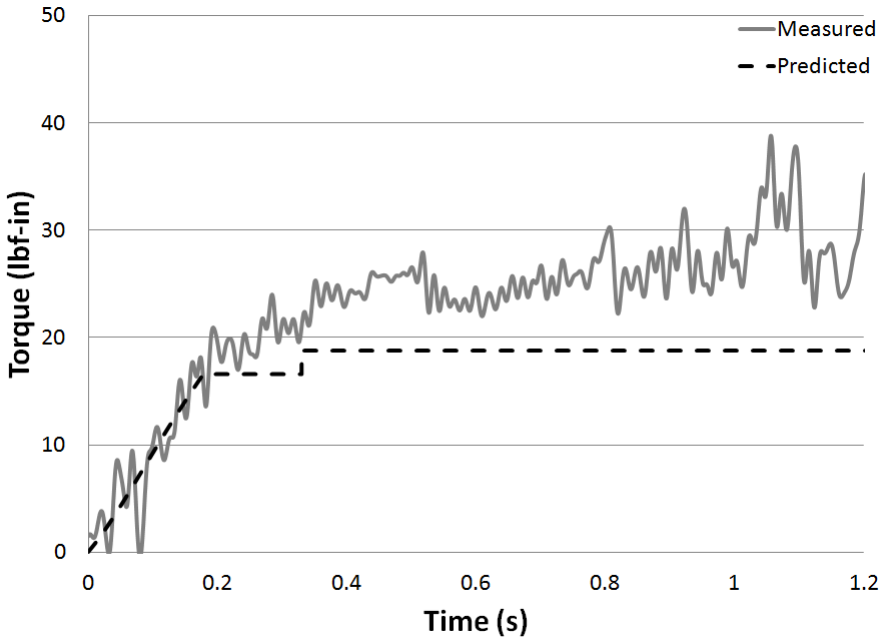

Figure 65: Predicted and Measured Torque: Speed 4000 rpm, Feed 0.008 ipr

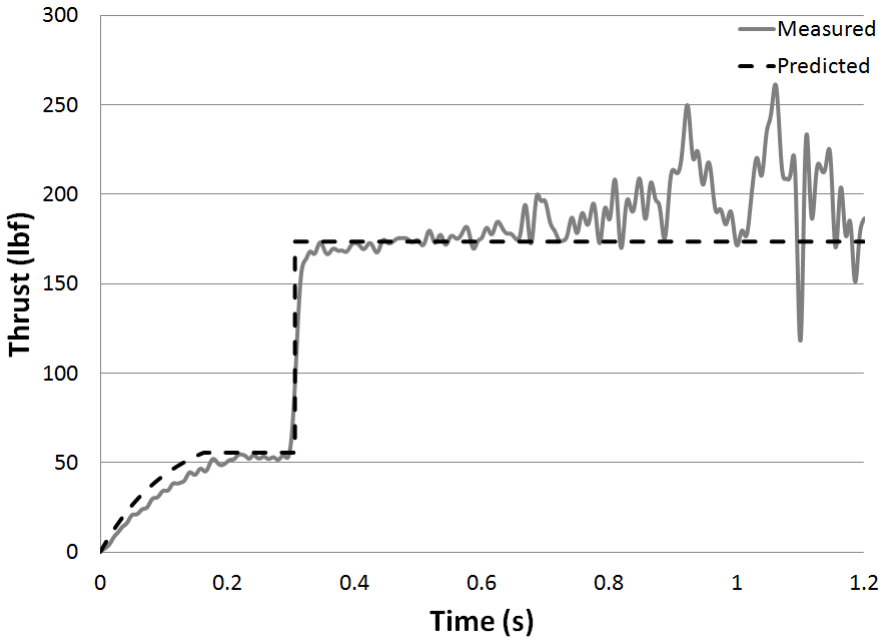

Figure 66: Predicted and Measured Thrust: Speed 5000 rpm, Feed 0.007 ipr

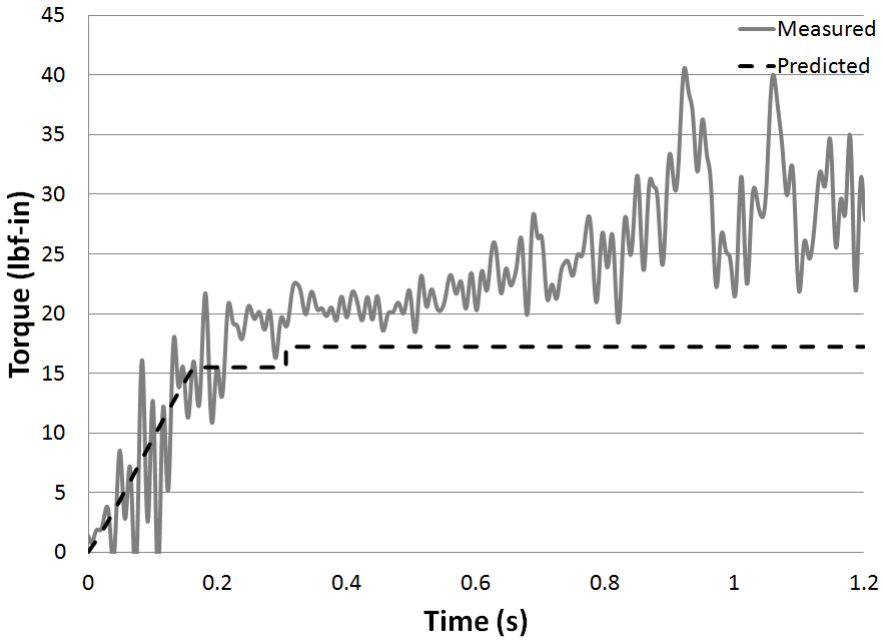

Figure 67: Predicted and Measured Torque: Speed 5000 rpm, Feed 0.007 ipr

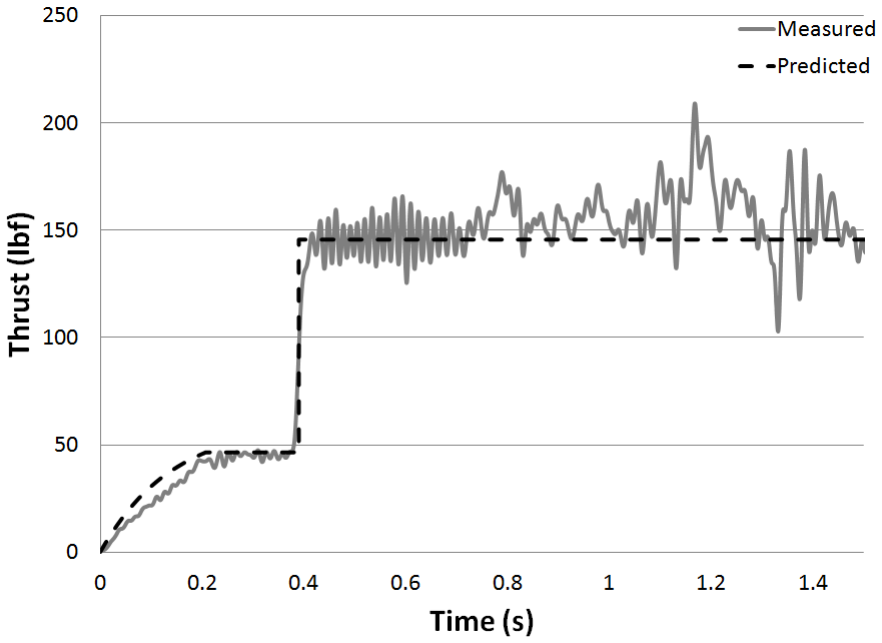

Figure 68: Predicted and Measured Thrust: Speed 5500 rpm, Feed 0.005 ipr

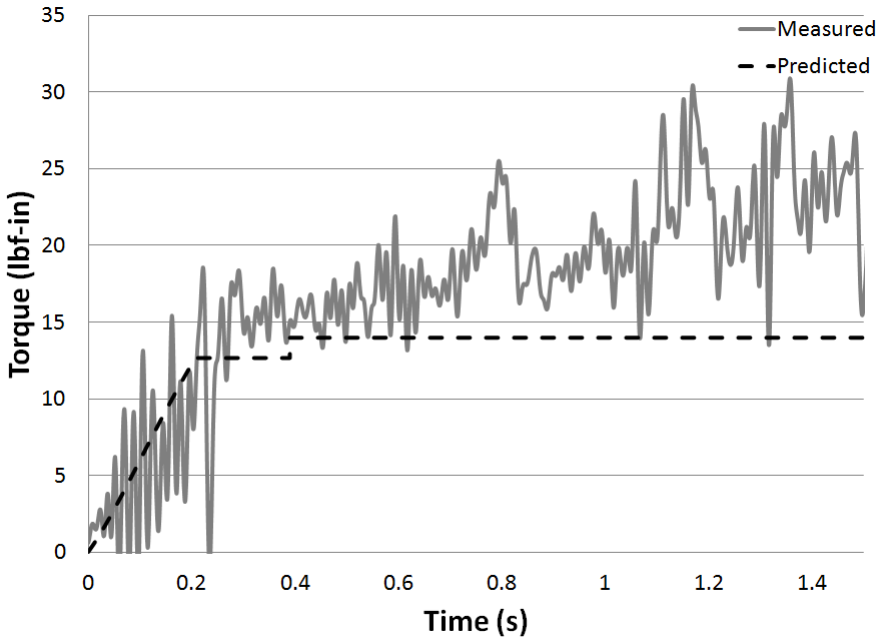

Figure 69: Predicted and Measured Torque: Speed 5500 rpm, Feed 0.005 ipr

APPENDIX C

STEP DRILL VALIDATION TESTS

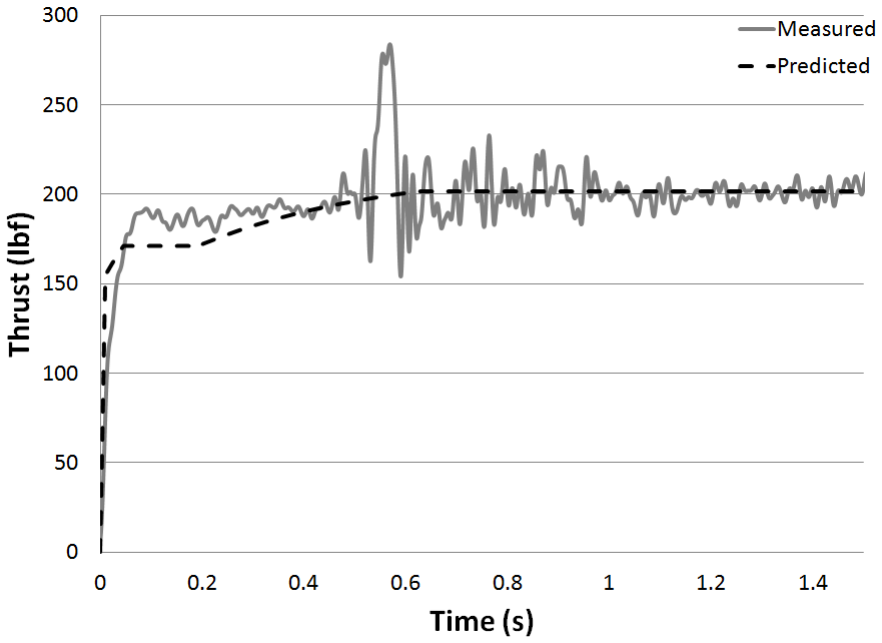

Figure 70: Predicted and Measured Thrust: Secondary Point Angle 60 degrees, Inner Diameter 0.1 in, Speed 3000 rpm, Feed 0.009 ipr

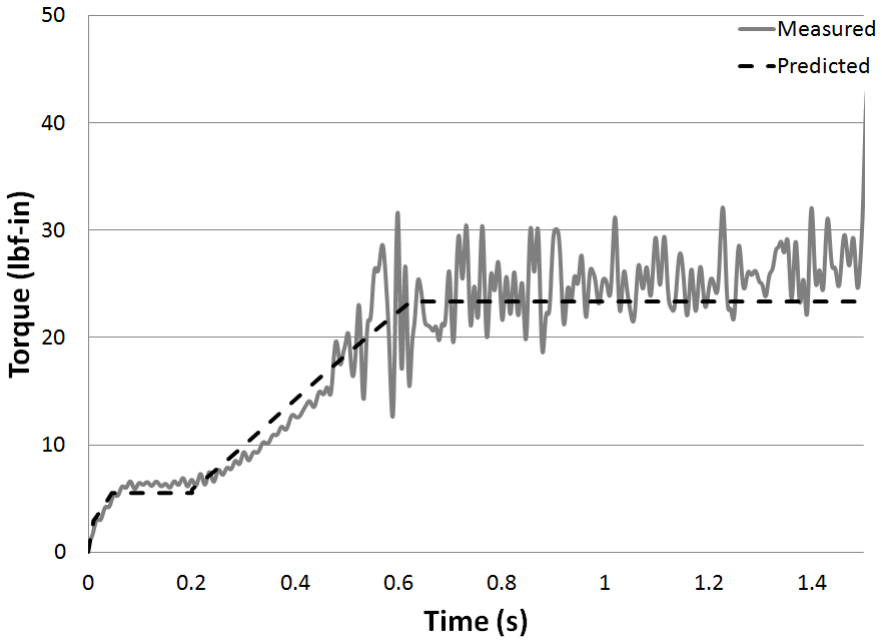

Figure 71: Predicted and Measured Torque: Secondary Point Angle 60 degrees, Inner Diameter 0.1 in, Speed 3000 rpm, Feed 0.009 ipr

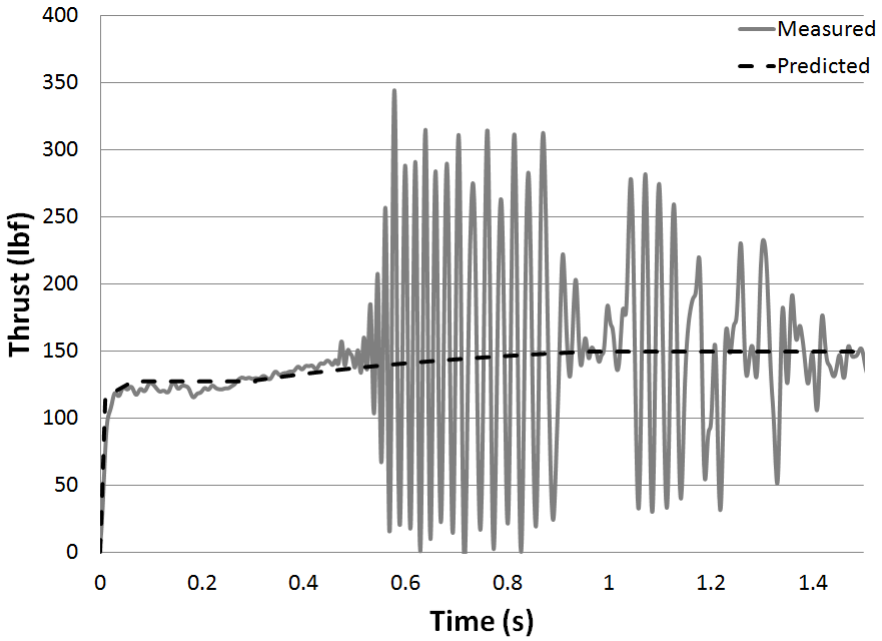

Figure 72: Predicted and Measured Thrust: Secondary Point Angle 60 degrees, Inner Diameter 0.1 in, Speed 5500 rpm, Feed 0.005 ipr

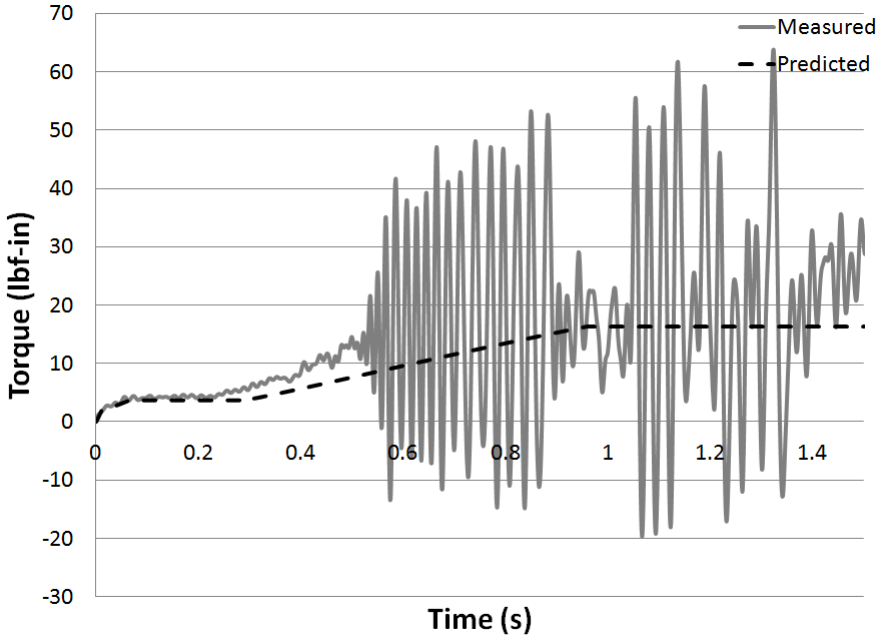

Figure 73: Predicted and Measured Torque: Secondary Point Angle 60 degrees, Inner Diameter 0.1 in, Speed 5500 rpm, Feed 0.005 ipr

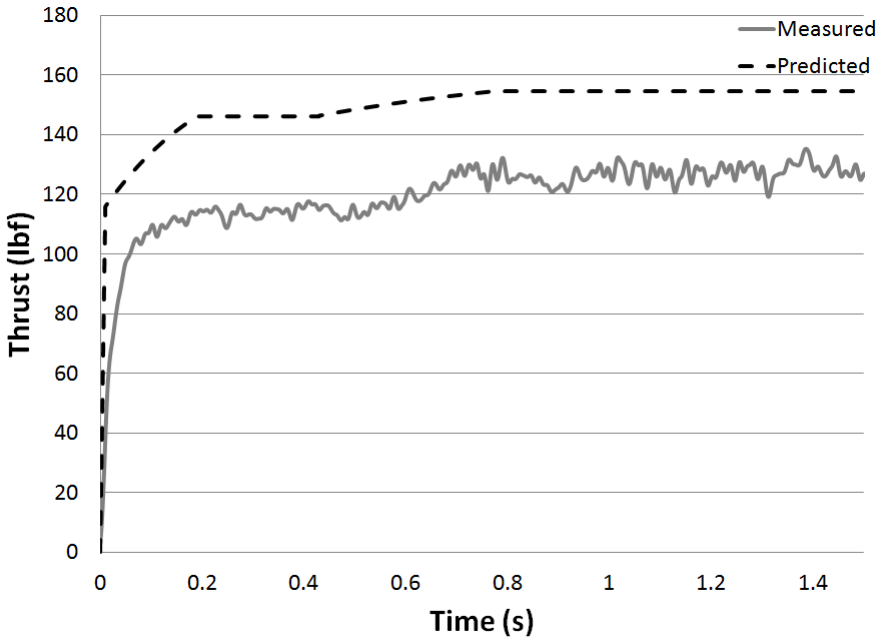

Figure 74: Predicted and Measured Thrust: Secondary Point Angle 60 degrees, Inner Diameter 0.2 in, Speed 3500 rpm, Feed 0.005 ipr

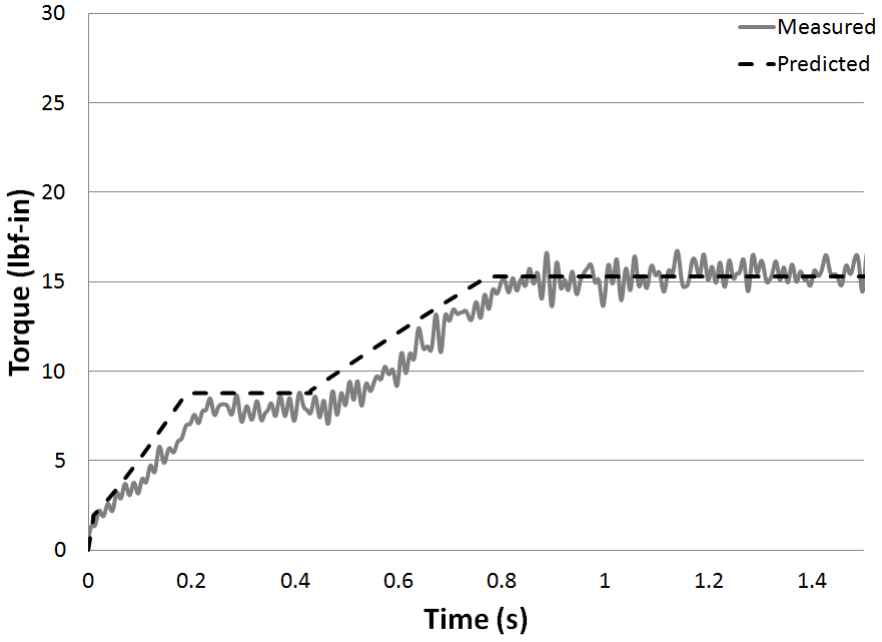

Figure 75: Predicted and Measured Torque: Secondary Point Angle 60 degrees, Inner Diameter 0.2 in, Speed 3500 rpm, Feed 0.005 ipr

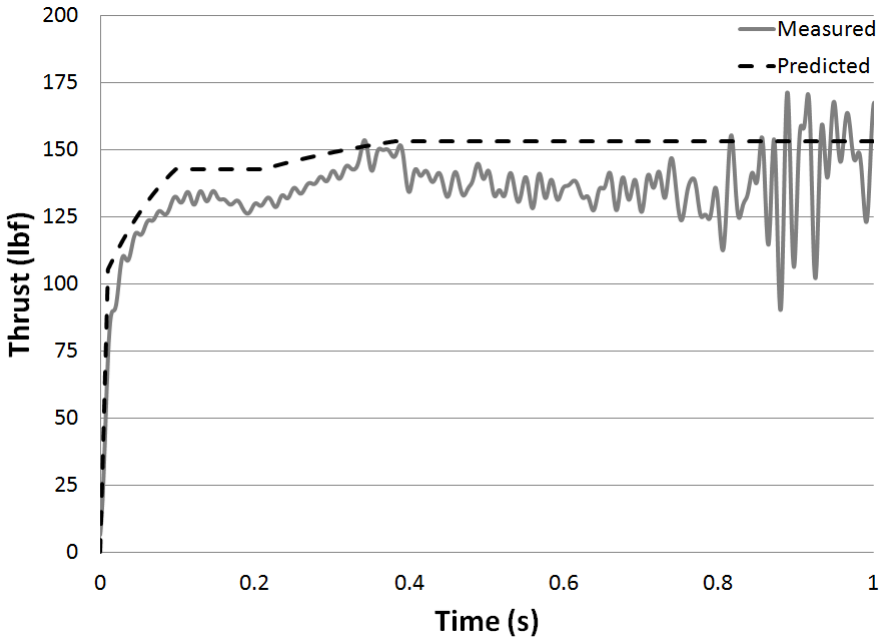

Figure 76: Predicted and Measured Thrust: Secondary Point Angle 60 degrees, Inner Diameter 0.2 in, Speed 6000 rpm, Feed 0.006 ipr

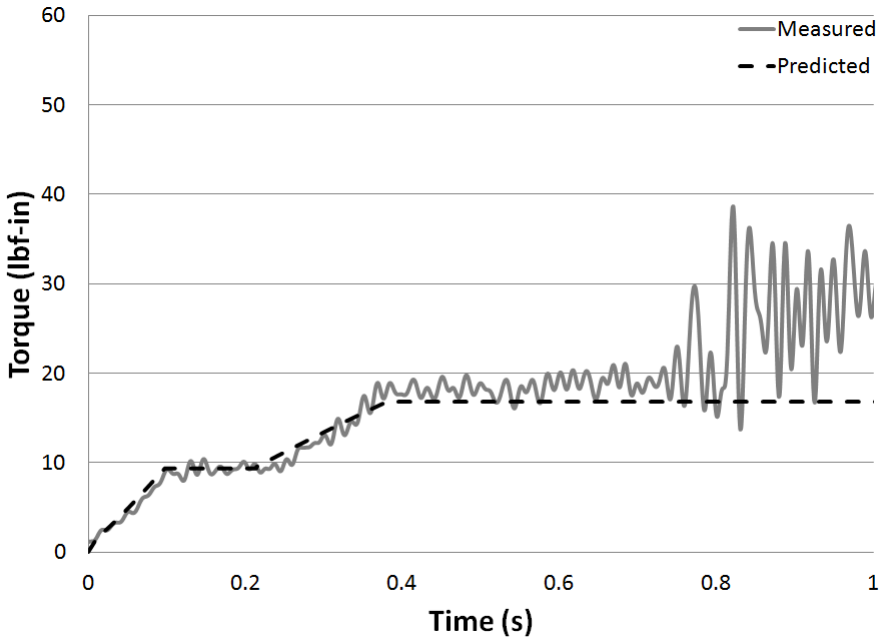

Figure 77: Predicted and Measured Torque: Secondary Point Angle 60 degrees, Inner Diameter 0.2 in, Speed 6000 rpm, Feed 0.006 ipr

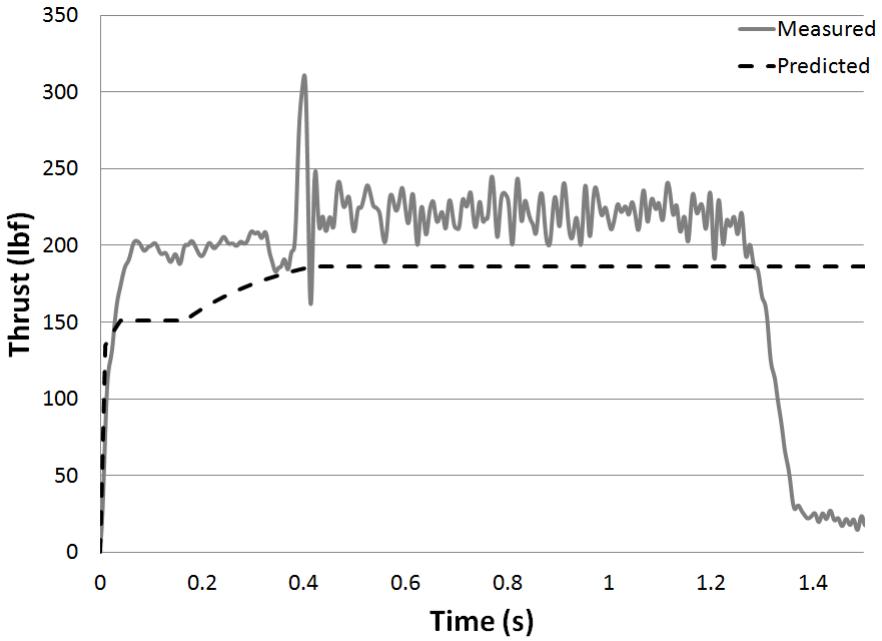

Figure 78: Predicted and Measured Thrust: Secondary Point Angle 80 degrees, Inner Diameter 0.1 in, Speed 4000 rpm, Feed 0.008 ipr

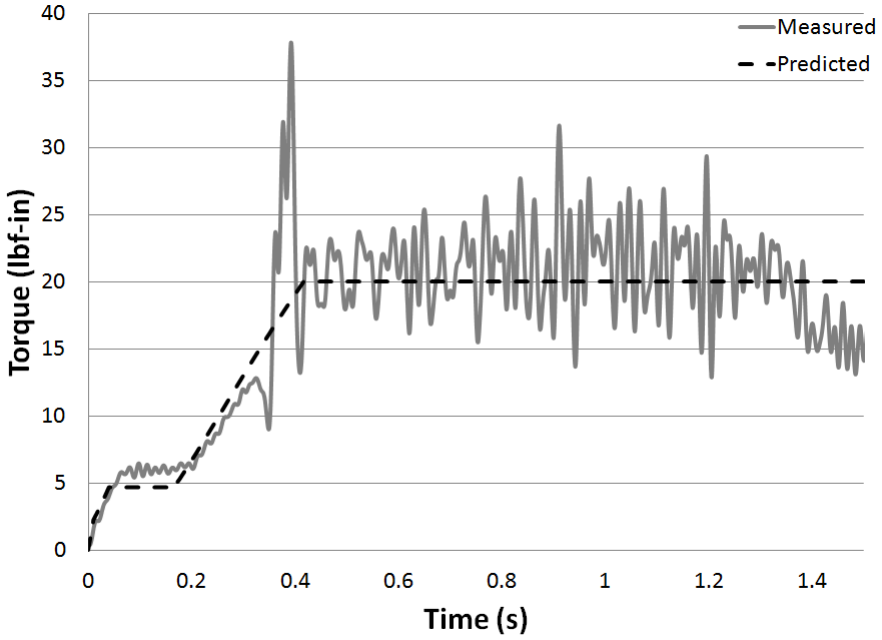

Figure 79: Predicted and Measured Torque: Secondary Point Angle 80 degrees, Inner Diameter 0.1 in, Speed 4000 rpm, Feed 0.008 ipr

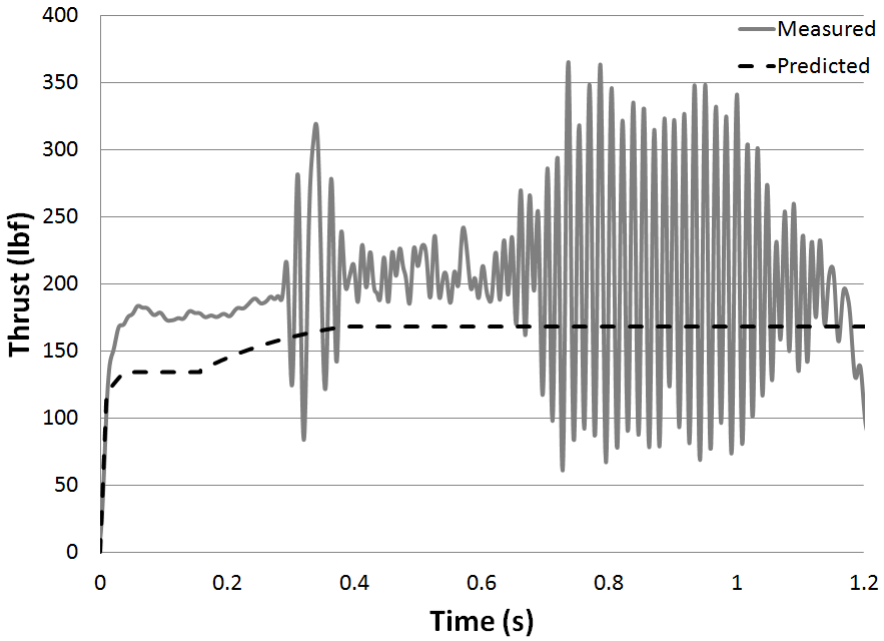

Figure 80: Predicted and Measured Thrust: Secondary Point Angle 80 degrees, Inner Diameter 0.1 in, Speed 5000 rpm, Feed 0.007 ipr

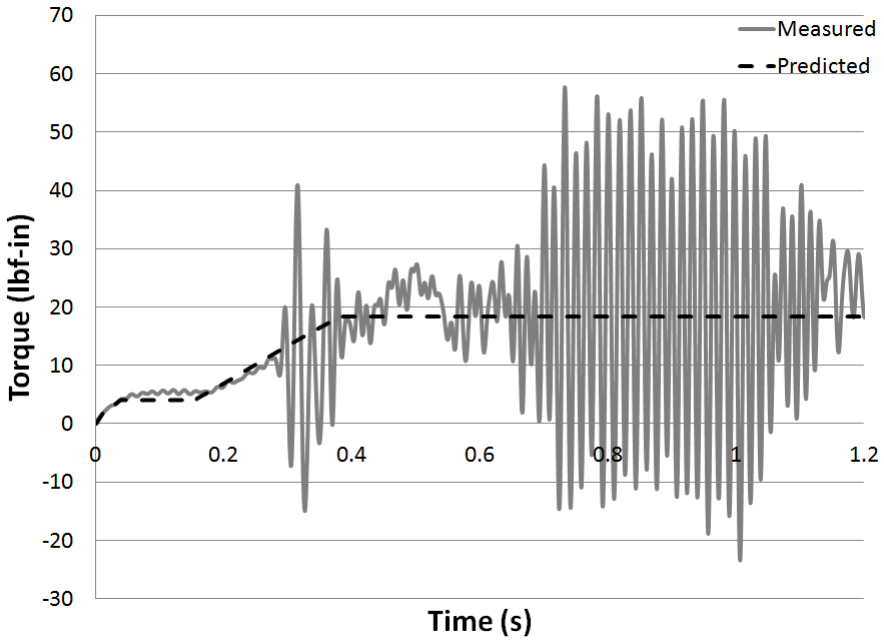

Figure 81: Predicted and Measured Torque: Secondary Point Angle 80 degrees, Inner Diameter 0.1 in, Speed 5000 rpm, Feed 0.007 ipr

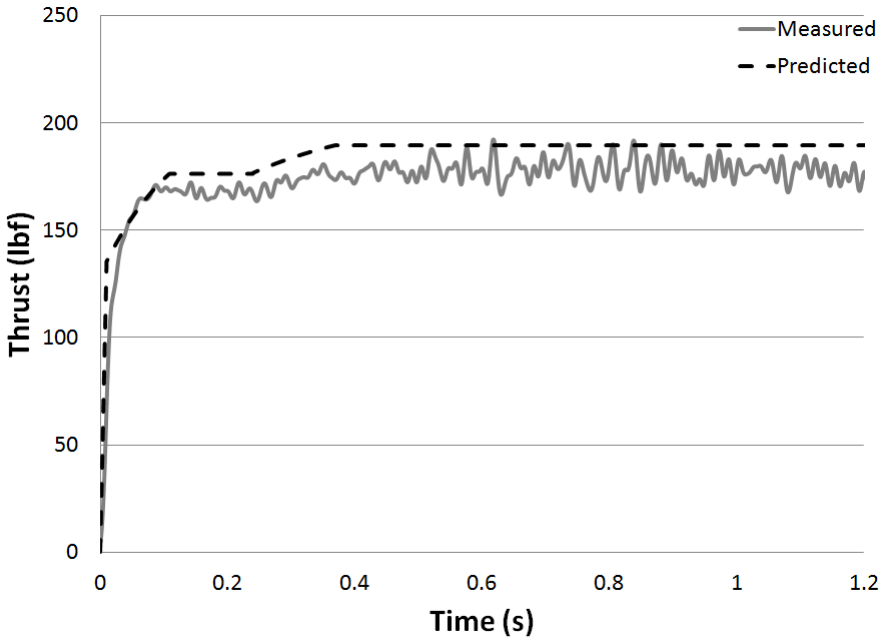

Figure 82: Predicted and Measured Thrust: Secondary Point Angle 80 degrees, Inner Diameter 0.2 in, Speed 4000 rpm, Feed 0.008 ipr

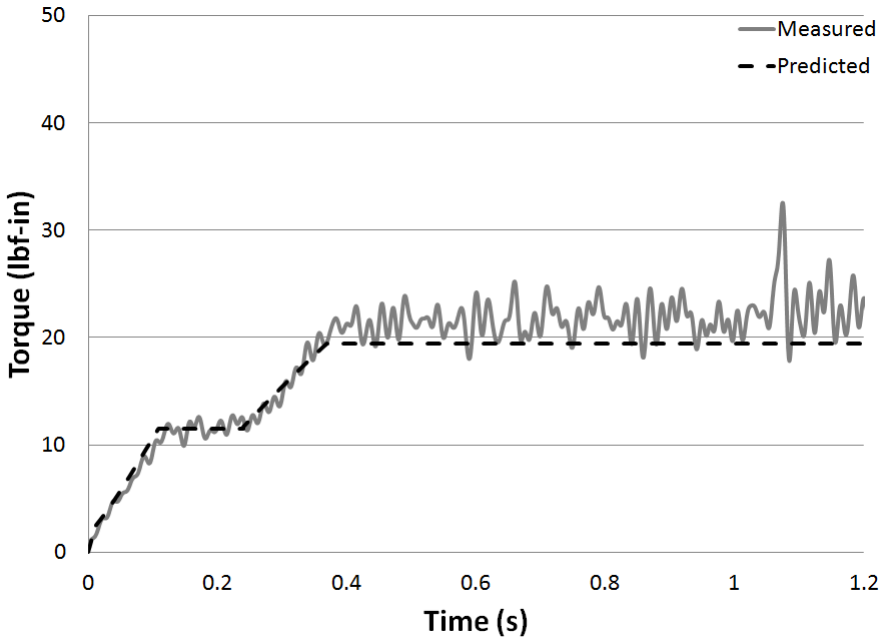

Figure 83: Predicted and Measured Torque: Secondary Point Angle 80 degrees, Inner Diameter 0.2 in, Speed 4000 rpm, Feed 0.008 ipr

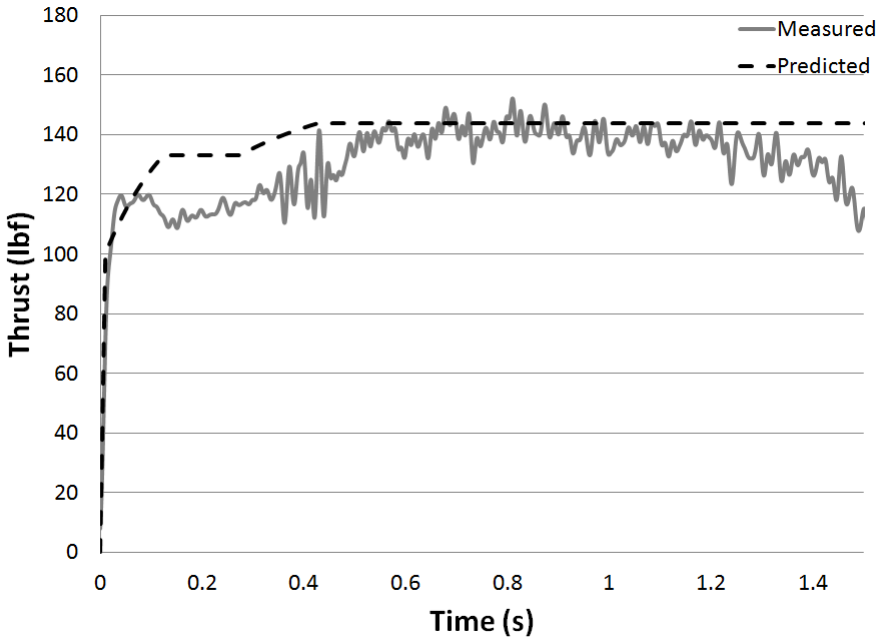

Figure 84: Predicted and Measured Thrust: Secondary Point Angle 80 degrees, Inner Diameter 0.2 in, Speed 5500 rpm, Feed 0.005 ipr

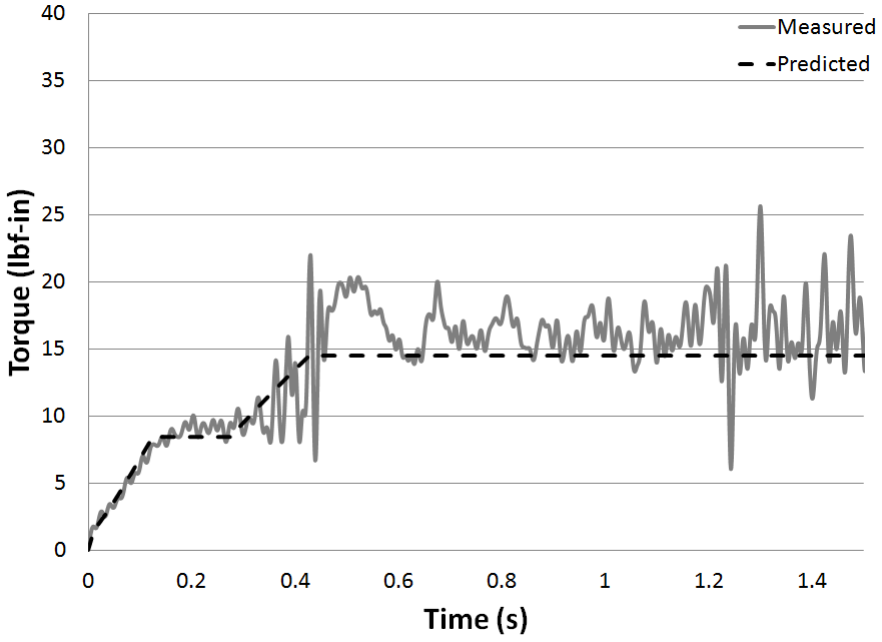

Figure 85: Predicted and Measured Torque: Secondary Point Angle 80 degrees, Inner Diameter 0.2 in, Speed 5500 rpm, Feed 0.005 ipr

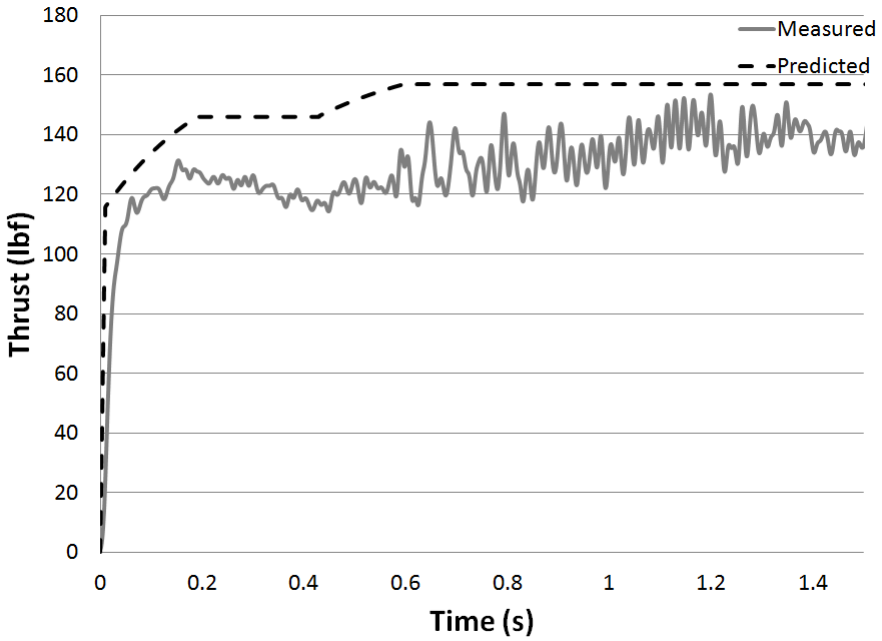

Figure 86: Predicted and Measured Thrust: Secondary Point Angle 100 degrees, Inner Diameter 0.2 in, Speed 3500 rpm, Feed 0.005 ipr

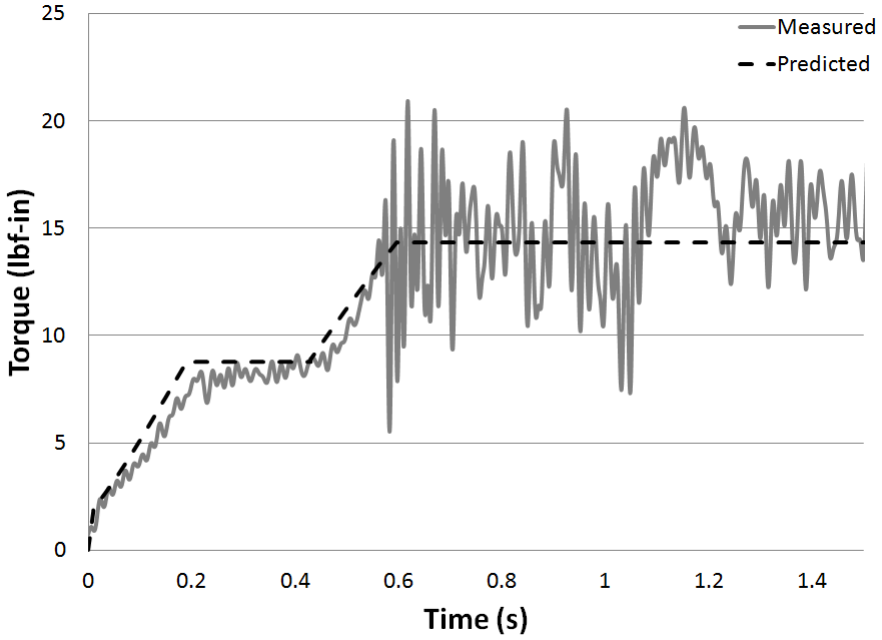

Figure 87: Predicted and Measured Torque: Secondary Point Angle 100 degrees, Inner Diameter 0.2 in, Speed 3500 rpm, Feed 0.005 ipr

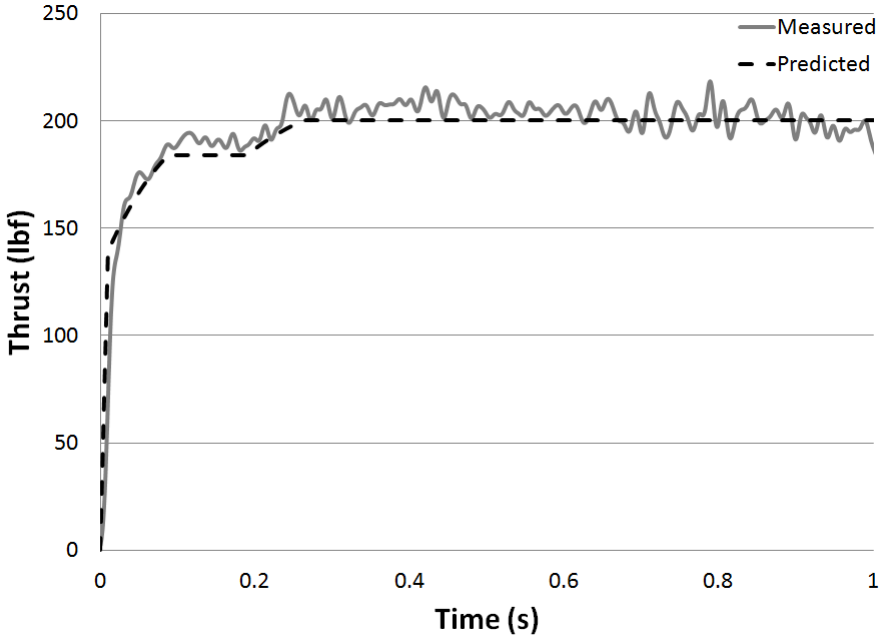

Figure 88: Predicted and Measured Thrust: Secondary Point Angle 100 degrees, Inner Diameter 0.2 in, Speed 4500 rpm, Feed 0.009 ipr

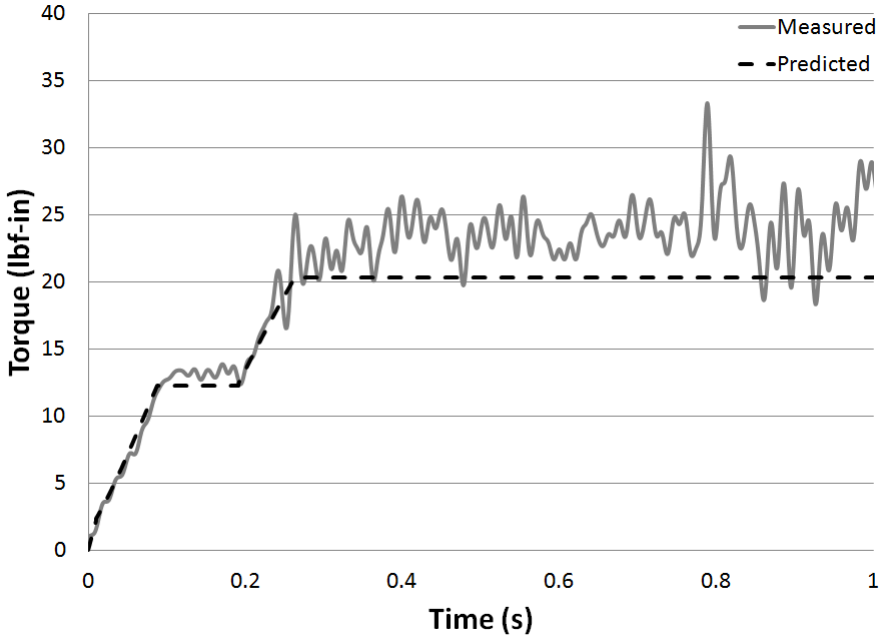

Figure 89: Predicted and Measured Torque: Secondary Point Angle 100 degrees, Inner Diameter 0.2 in, Speed 4500 rpm, Feed 0.009 ipr

REFERENCES

[1] Armarego, E. J. A., "A generic mechanics of cutting approach to predictive technological performance modelling of the wide spectrum of machining operations," *Mach. Sci. Technol.*, vol. 2, pp. 191–211, Dec. 1998.

[2] Chandrasekharan, V., "A mechanistic model for predicting the thrust and torque in drilling: With application to fiber-reinforced composite materials," Master's thesis, University of Illinois at Urbana-Champaign, Urbana, Illinois, 1993.

[3] Constantin, C., Croitoru, S. M., Constantin, G., and Bisu, C. F., "3D FEM Analysis of Cutting Processes," in *3rd WSEAS International Conference on Visualization, Imaging and Simulation*, pp. 41–46, World Scientific and Engineering Academy and Society, 2010.

[4] de Lacalle, L. N. L., Rivero, A., and Lamikiz, A., "Mechanistic model for drills with double point-angle edges," *Int. J. Adv. Manuf. Technol.*, vol. 40, no. 5–6, pp. 447–457, 2009.

[5] Gaitonde, V., Karnik, S., Achyutha, B., and Siddeswarappa, B., "Genetic algorithm-based burr size minimization in drilling of aisi 316l stainless steel," *J. Mater. Process. Technol.*, vol. 197, no. 1–3, pp. 225–236, 2008.

[6] Gong, Y., Lin, C., and Ehmann, K. F., "Dynamics of initial penetration in drilling: Part 1-mechanistic model for dynamic forces," *J. Manuf. Sci. Eng.*, vol. 127, no. 2, pp. 280–288, 2005.

[7] Hellstern, C., "Investigation of interlayer burr formation in the drilling of stacked aluminum sheets," Master's thesis, Georgia Institute of Technology, Atlanta, Georgia, 2009.

[8] Isbilir, O. and Ghassemeih, E., "Finite element analysis of drilling titanium alloy," *Procedia Engineering*, vol. 10, pp. 1877–1882, 2011.

[9] Kachanov, L. M., *Foundations of the Theory of Plasticity.* North-Holland, 1971.

[10] Kapoor, S. G., DeVor, R. E., Zhu, R., Gajjela, R., Parakkal, G., and Smithey, D., "Development of mechanistic models for the prediction of machining performance: Model-building methodology," *Mach. Sci. Technol.*, vol. 2, pp. 213–238, Dec. 1998.

[11] Karnik, S., Gaitonde, V., and Davim, J., "A comparative study of the ann and rsm modeling approaches for predicting burr size in drilling," *Int. J. Adv. Manuf. Technol.*, vol. 38, no. 9–10, pp. 868–883, 2008.

[12] Kilickap, E. and Huseyinoglu, M., "Selection of optimum drilling parameters on burr height using response surface methodology and genetic algorithm in drilling of aisi 304 stainless steel," *Mater. Manuf. Processes*, vol. 25, no. 10, pp. 1068–1076, 2010.

[13] Kim, J. and Dornfeld, D. A., "Development of an analytical model for drilling burr formation in ductile materials," *J. Eng. Mater. Technol.*, vol. 124, no. 2, 2002.

[14] Ko, S. L., Chang, J. E., and Kalpakjian, S., "Development of drill geometry for burr minimization in drilling," *CIRP J. Manuf. Sci. Technol.*, vol. 52, no. 1, pp. 45–48, 2003.

[15] Ko, S. L., Chang, J. E., and Yang, G. E., "Burr minimizing scheme in drilling," *J. Mater. Process. Technol.*, vol. 140, pp. 237–242, Sept. 2003.

[16] Ko, S. L. and Lee, J. K., "Analysis of burr formation in drilling with a new-concept drill," *J. Mater. Process. Technol.*, vol. 113, pp. 392–398, June 2001.

[17] Ma, L., Marusich, T. D., Usui, S., Wadell, J., Marusich, K., Zamorano, L., and Elangovan, H., "Validation of finite element modeling of drilling processes with solid tooling in metals," *Advanced Materials Reserach*, vol. 223, pp. 182–190, 2011.

[18] Mauch, C. A. and Lauderbaugh, L. K., "Modeling the drilling process. an analytical model to predict thrust force and torque," *ASME MD*, vol. 20, pp. 59–65, 1990.

[19] Min, S., Dornfeld, D. A., Kim, J., and Shyu, B., "Finite element modeling of burr formation in metal cutting," *Mach. Sci. Technol.*, vol. 5, no. 3, 2001.

[20] Oxford, Jr., C. J., "On the drilling of metals – 1. basic mechanics of the process," *ASME Transactions*, vol. 77, pp. 103–111, Feb. 1955.

[21] Pande, S. and Relekar, H., "Investigations on reducing burr formation in drilling," *Int. J. Mach. Tool Design and Research*, vol. 26, no. 3, pp. 339–348, 1986.

[22] Paul, A., Kapoor, S. G., and DeVor, R. E., "Chisel edge and cutting lip shape optimization for improvved twist drill point design," *Int. J. Mach. Tool. Manuf.*, vol. 45, no. 4–5, pp. 421–31, 2005.

[23] Ramu, C., Mehta, N., Kumar, P., and Murthy, A., "Experimental investigations to optimise step drill geometry for burr minimisation in drilling using regression model," *Int. J. Manuf. Tech. and Management*, vol. 21, no. 1–2, pp. 122–34, 2010.

[24] Sabberwal, A. J. P., "Chip section and cutting force during the milling operation," *Annals of the CIRP*, vol. 10, no. 3, pp. 197–203, 1961.

[25] Schlesinger, G., "Cutting angle of twist drills," *Engineer*, vol. 166, no. 4326, pp. 650–651, 1938.

[26] Sheng, Y. and Tomizuka, M., "Intelligent modeling of thrust force in drilling process," *J. Dyn. Syst. Meas. Contr.*, vol. 128, no. 4, pp. 846–855, 2006.

[27] Xia, R. S. and Mahdavian, S. M., "Experimental studies of step drills and establishment of empirical equations for the drilling," *Int. J. Mach. Tools Manuf*, vol. 45, pp. 235–240, Feb. 2005.